INSTITUTO SUPERIOR TÉCNICO
Universidade Técnica de Lisboa

Liver Tumor Classification based on DCE-MRI Images

Nuno Miguel da Silva Mendes Pedrosa de Barros

Dissertação para a obtenção de Grau de Mestre em
Engenharia Biomédica

Júri

Presidente:	Prof. Paulo Freitas
Orientador:	Prof. João Sanches
Vogal:	Prof. Patrícia Figueiredo
Vogal:	Prof. Rui Tato Marinho

October 2010

Acknowledgements

Resumo

A Ressonância Magnética com contraste dinâmico tem demonstrado ser o método de diagnóstico mais eficiente na detecção de tumores hepáticos. Esta técnica de imagem permite avaliar a perfusão tecidual através do seguimento da difusão de um contraste intravenoso no corpo humano.

As capacidades imagiológicas desta técnica podem ser consideravelmente melhoradas através da modelação da informação contida na imagem com modelos farmacocinéticos que descrevem o processo de difusão do contraste. A aplicação de tais modelos permite recolher diversos parâmetros de perfusão.

O fígado é caracterizado por um duplo aporte sanguíneo: 75% do sangue que entra no fígado tem a sua origem na veia porta hepática e os restantes 25% na artéria hepática. No entanto, este equilíbrio pode ser alterado localmente ou globalmente em diversas condições patológicas, como por exemplo no cancro do fígado. Desta forma, a estratégia principal utilizada nesta tese para avaliar diferenças entre tumores do fígado consistiu na medida da percentagem arterial do tecido tumoral. Isto implica a utilização de um modelo de perfusão hepática com dupla entrada, onde a perfusão do fígado é calculada com base nos sinais recolhidos da aorta e da veia porta.

O modelo foi implementado em MATLAB e uma interface gráfica foi criada.

Seis casos com diagnóstico confirmado pelo hospital Erasme, em Bruxelas, foram analisados usando o método descrito. Estes estudos imagiológicos continham um total de 9 tumores, incluindo 4 tumores benignos e 5 carcinomas. O modelo usado permitiu recolher uma quantidade considerável de parametros de perfusão à parte da percentagem arterial.

Apesar de terem sido usadas imagens com fraca resolução temporal, o método foi capaz de detectar diferenças claras entre tumores benignos e malignos em termos da percentagem arterial. Os resultados confirmaram o facto de os carcinomas hepáticos serem maioritariamente alimentados pela artéria hepática. Os tumores benignos registaram percentagens arteriais médias entre 16.6% e 37.5%. Contrariamente, os tumores malignos revelaram uma componente arterial num intervalo entre 51.4% e 75.5%.

Abstract

Dynamic Contrast Enhanced Magnetic Resonance Imaging has proven to be the most efficient diagnose method for liver tumor identification. This image technique allows assessing tissue perfusion by following the diffusion of an intravenous contrast agent in the human body.

DCE-MRI imaging capabilities can be considerably increased by modeling the imaging data acquired with pharmokinetic models that describe the contrast diffusion process. The application of such models allows retrieving several perfusion parameters.

The liver is characterized by a dual-blood supply: 75% of the blood that enters the liver has its origin in the hepatic portal vein and the rest 25 % in the hepatic artery. However, this balance can be altered locally or globally in several pathological conditions, like for example in liver cancer. So, the main strategy used in this thesis to assess differences between liver tumors consisted in the measurement of the arterial ratio of tumor tissue. This implied the use of a dual-input liver perfusion model, where the hepatic perfusion is calculated based on the signals retrieved from the aorta and the portal vein.

The model was implemented in MATLAB and a Graphical User Interface was created.

Six cases with confirmed diagnosis given by the hospital Erasme, in Brussels, were analyzed using the method described. These imaging studies contained a total of 9 tumors, including 4 benign tumors and 5 carcinomas. The model used allowed collecting a considerable amount of perfusion parameters apart from the arterial ratio.

Besides using low temporal images, the method was able to detect clear differences between benign and malignant tumors in terms of the arterial ratio. The results confirmed the fact of liver carcinomas being mostly supplied by the hepatic artery. Benign tumors registered mean arterial ratios between 16.6% and 37.5%. On the contrary, malignant tumors revealed an arterial component in a range between 51.4% and 75.5%.

Contents

List of Tables

List of Figures

Abbreviations

CT	*Computed Tomography*
DCE-MRI	*Dynamic Contrast Enhanced Magnetic Resonance Imaging*
EES	*Extravascular Extracellular Space*
FFD	*Free Form Deformations*
GUI	*Graphical User Interface*
HCC	*Hepatocellular Carcinoma*
IARC	*International Agency for Research on Cancer*
MI	*Mutual Information*
MR	*Magnetic Resonance*
MRF	*Markov Random Field*
NMI	*Normalized Mutual Information*
ROI	*Region of Interest*
VOI	*Volume of Interest*

Chapter 1

Introduction

Liver cancer is a silent killer: usually detection occurs when there is nothing left to do. According to the IARC(International Agency for Research on Cancer) Globocan 2008 project, liver cancer killed 478,275 persons worldwide and 522,355 new cases were registered in 2008. In the same year, in Europe, an incidence of 46,566 cases and a mortality of 46,483 Europeans were observed [15]. This proximity between incidence and mortality values reveals how deadly liver cancer is. The geographic distribution of this disease (figure 1.1) is intrinsically connected to the occurrence and natural history of Hepatitis B and C ([3],[4]). Consequently, vaccination against these viruses reveals to be essential for liver cancer prevention. However, in the fight against this type of cancer screening plays a very important role. In 2004, a Chinese study with 18,816 patients reported that biannual screening was able to reduce hepatocellular carcinoma (HCC) mortality by 37%, being this the most common primary liver cancer[57].

Large tumors can be easily identified by several imaging techniques. However, late detection does not save lives. In order to improve survival, liver cancer has to be detected in an early stage, when its smaller dimensions and less marked features make difficult its identification. Dynamic Contrast Enhanced Magnetic Resonance Imaging (DCE-MRI) has proven to be the most efficient diagnostic method for liver tumor identification([14],[48],[55]). Despite the elevated price of this imaging technique, efforts are being made to reduce the related costs and its availability is increasing. This reveals to be important taking into account that its noninvasiveness makes it ideal for screening applications. Moreover, its capabilities can be considerably increased when image processing comes into action. DCE-MRI provides a huge amount of data whose computational analysis allows not only highlighting differences between normal and pathological cases, but also reveal important information that in a human-based analysis would be unnoticed. This thesis is presented in the context of liver cancer imaging improvement by the application of image processing techniques to DCE-MRI images.

The approach here developed is based upon pharmacokinetic analysis. More specifically, by means of studying how the contrast diffuses in the patient's body and modeling the data with pharmacokinetic models, a certain group of parameters are retrieved. These parameters are a reflex of the perfusion properties of the region imaged. Thus, since perfusion is altered in neoplasic situations it is intended to analyze how malign features are traduced in the perfusion parameters collected. This form the basis on which this thesis develops.

At ISR (Instituto de Sistemas e Robótica), a first approach on this type of image processing had already been made by Caldeira L. *et al.*. The research made obtained interesting results, having been capable of detecting differences in the speed of contrast uptake and downtake between benign and malign tumors. However, pharmacokinetic analysis has shown to have greater potentialities and a lot was left to explore. One of the points where this work distinguishes from the previous is due to the consideration of liver dual-blood supply. The liver is a unique organ in the sense that it receives blood from both a venous and an arterial sources. In normal conditions about 75% of the incoming
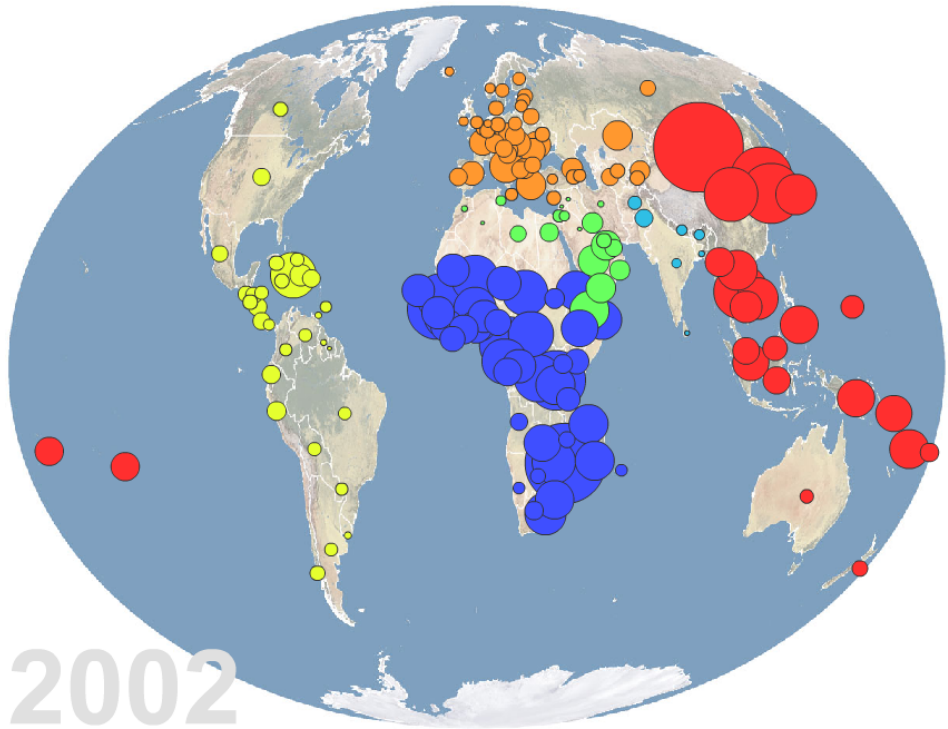
Figure 1.1: Worldwide distribution of liver cancer in men. The size of each circle placed among every country is proportional to the number of new cases of liver cancer per 100,000 male residents during 2002. The greatest incidence rate is observed in Mongolia where 57 new cases per 100,000 male residents were found in 2002 and the smallest in Guyana where the same indicator has a value of 0.2. In Portugal the number of new cases is relatively small with 1.8 new cases per 100,000 male habitants in 2002. The image was obtained using Gapminder and the incidence data was compiled also by Gapminder using data from IARC GLOBOCAN 2002 (estimates for 2002) and IARC CI5 (Cancer Incidence in 5 Continents) time series data.

blood comes from the portal vein and the rest 25% from the hepatic artery. However, this balance can be altered locally or globally in several pathological conditions, such as in liver cancer or cirrhosis. Based on this, the method used was developed in order to be able to resolve hepatic portal venous and arterial components of blood flow. In parallel, several other perfusion characteristics can be assessed. The analysis was made in a voxel-by-voxel approach, which allows building parameter maps that can facilitate tumor detection and also identify tumor characteristic heterogeneity.

1.1 Thesis Organization

This thesis is organized in four chapters:

- **Background**, is presented the main theoretical background information that constitutes the basis of this work. Here one can find: information concerning the imaging technique (DCE-MRI), a brief reference the most common tumors found in liver and a description of the evolution of perfusion models related to the one applied here. There are also mentioned the important features of the liver in the contrast imaging perspective, the theory behind the software used to perform the fundamental

task of image alignment and the acquisition characteristics of the images used in this thesis.

- **Method**. In this chapter the method used to reach our initial goals is described. Here the algorithm is approached first in a general basis and then component by component.

- **Interface**. Here is shown the user-interface developed to improve the interaction between the algorithm, the imaging data and the user. In this chapter is presented a more practical view of how the methods described previously can be implemented.

- **Results**. After the description of the theory behind the method, the method itself and its implementation, the results obtained are revealed and their meaning discussed.

- **Conclusions and Future Work**. Finally, the main conclusions are exposed as the future perspectives that resulted from this thesis.

Chapter 2

Background

2.1 Dynamic Contrast Enhanced Magnetic Resonance Imaging

Briefly, DCE-MRI consists of the acquisition of several Magnetic Resonance images at different instances in time, after a contrast substance being introduced in the patient's blood flow. This ties the MRI imaging capabilities with the perfusion information given by the contrast variation in each tissue.

Since its introduction in oncology, DCE-MRI has assisted doctors with non-invasive methods to: identify and classify lesions, follow-up patients, assess their response to treatment and screen risk populations.

DCE-MRI images have demonstrated its superiority in the differential diagnosis between malignant and benign lesions in comparison with other imaging techniques such as ultrasound[25] and CT[14]. Even so, this performance difference it's not so well-marked in terms of lesion detection[48].

Dynamic contrast MRI is distinguished by its capability to detect alterations in tissue contrast enhancement patterns, making it particularly useful in oncology, since tumor growth tends to modify normal tissue perfusion characteristics in several ways. Consequently, small avascular tumors are undetectable with this imaging technique.

Perfusion characteristics or physiological data may be extracted from DCE-MRI studies by the application of pharmacokinetic models that mimic contrast distribution processes in the human body.

In malignant tumors an abnormal development with lack of vascular structural maturation is observed. This results in a heterogeneous, high permeable and fragile structure formed by coarse capillaries[20]. In benign tumors angiogenesis comes with normal maturation and consequently a more regular and homogeneous vasculature is obtained. Therefore, in DCE-MRI images malignant tumors normally reveal faster intensity changes with higher amplitude, in comparison with normal tissue and other less malignant or benign tumors [37]. According to tumor size and image resolution, heterogeneity in malign tumors may be or not detectable.

The contrast injection is usually performed in a peripheral vein by means of an automated procedure to ensure reproducibility. The coherency of the bolus is assured by the immediate injection of normal saline at the same rate of the previous injection.

Most of the contrast agents used are classified into three main groups: low molecular weight agents, with less than 1000 Dalton that easily diffuse to the extravascular-extracellular space (EES); large-molecular weight agents with more than 30,000 Dalton that are retained inside vessels (blood pool agents or macromolecular contrast media); and contrasts designed to accumulate in sites with active angiogenesis. In the specific case of the liver, there are contrast agents that are absorbed by the hepatocytes and excreted into the biliary tract; and others that are retained in the reticuloendothelial system and therefore can differentiate tumors based on the presence of Kupfer cells[2].
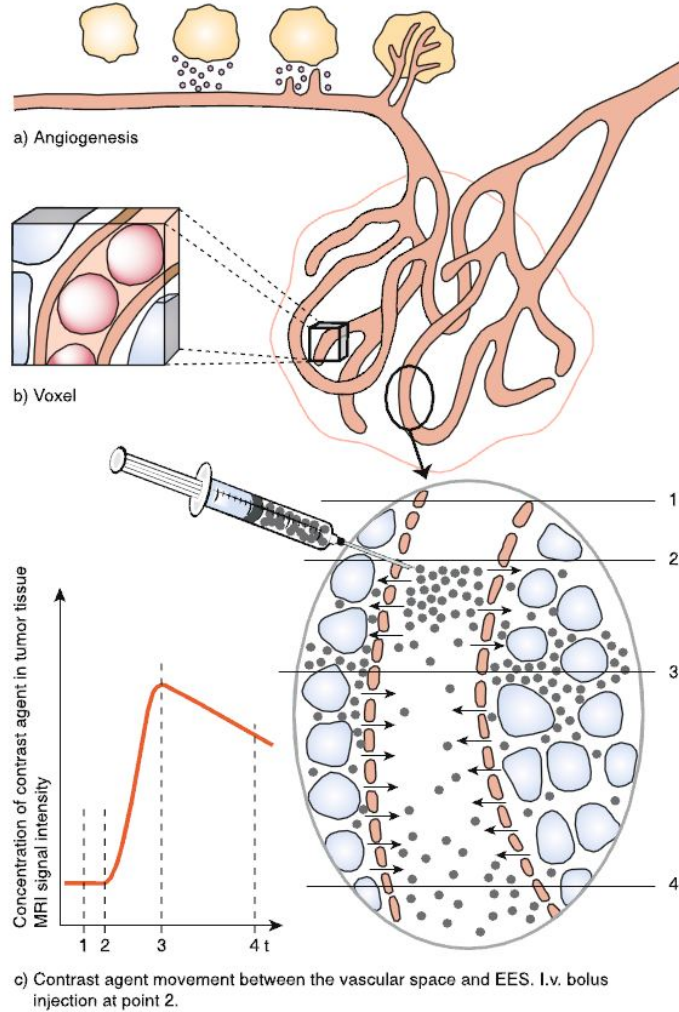
Figure 2.1: Overall view of the DCE-MRI technique baseline processes. In $a)$ a representation of the angiogenesis process with the respective sprout of new vessel from existing ones is shown. In $b)$ the concept that one voxel represents a determined volume that can contain several cells and capillaries is represented. Finally, in $c)$ the pharmacokinetic processes ruling the contrast agent diffusion between the EES and the vascular space are shown. This figure was obtained from [18].

Dynamic contrast MRI studies were made possible only recently with the emergence of new rapid acquisition protocols that, due to the increased temporal resolution, allowed following contrast variations through time.

Dynamic Contrast MRI can be either T1-weighted, relaxivity-based methods, or T2-weighted, susceptibility-based methods. In the first approach Gd induces a signal enhancement causing voxels to brighten as the corresponding tissue increases its contrast concentration. Contrary, in the latter methods the opposite phenomenon is observed with smaller amplitude.

T1-weighted methods are able to measure capillary surface area, transendothelial permeability, leakage space, transfer and rate constants and assess microvessel density. As so, these are used for lesion detection and characterization, predict and monitor response to treatment, determine tumor

6

staging and follow-up patients.

The T2-weighted based-techniques normally work with relative quantification methods and are mainly used to assess blood flow and volume, transit time, tumor grade and microvessel vessel density. These methods allow characterization of lesions mainly in breast, liver and brain. In terms of the brain, noninvasive brain tumor classification, direct brain tumor biopsy and treatment monitoring are permitted with this technique.

There are several imaging protocols suitable for DCE-MRI. The pulse sequence chosen should represent the best equilibrium possible between the concurrent choices of the spatial and temporal resolutions, Field-Of-View, Signal to Noise Ratio and degree of contrast weighting [18]. T1-weighted techniques normally use gradient echo-based sequences.

As it will be discussed later, the images used in this thesis are T1-weighted and, in order to achieve the spatial resolution and speed required, mainly use two methodologies: Keyhole and Parallel imaging. The first one is simply based on the fact that the central part of the k-space, where one finds the low spatial frequencies, will have most of the contrast image data contained on it. On the other hand, the outer lines of the k-space represent the high-frequency domain that will be mostly related with the structural image information and that in a breath-hold acquisition can be considered constant. As so, in order to increase temporal resolution one can simply acquire several times the central k-space and perform only one longer complete acquisition, during a single breath-hold. The same objective is shared by parallel imaging that consists of using several smaller coils, instead of only one bigger, to simultaneously receive data that combined will form the final image. This technique has the advantage of allowing rapid volume acquisition.

In every part of the body, the utility of MRI is related with the ability to maximize differences between normal and disease cases. In terms of the liver, fat suppression techniques allow increasing image contrast and are essential in tissue characterization and pathology identification of fatty livers.

One of the specific features of the liver, that is used to differentiate lesions, is its characteristic dual-blood supply: liver receives about 75% of its blood supply from the portal vein and the rest 25% from the hepatic arteries([11],[46]) (figure 2.2). This feature is also observed in some lesions that have its origin in normal liver tissue. However, in some cases lesions present a blood supply that contrasts with the one from the normal liver, causing these to show different enhancement patterns. In order to detect this differences, liver DCE-MRI is usually acquired in four different phases: pre-contrast, before contrast injection; arterial phase, during arterial 'first-pass' where the arterial blood with a high contrast concentration reaches the cells(see figure 2.1); portal phase, during venous 'first-pass' where a second amount of contrast arrives at the liver via the hepatic portal vein; and equilibrium, when the concentration in the EES is supposed to be greater than the one found in the capillaries. These multiphasic studies are produced with low temporal resolution in comparison with other techniques, being the images acquired at each specific phase.

The use of pharmacokinetic approaches in the liver should overcome mainly two distinct problems: the abdominal movement, largely caused by respiratory motion; and the dual-blood supply that should be considered in the model used. In terms of the respiratory motion, the effects are reduced by acquiring the images while the patient holds his breath. However, there are visible differences between distinct breatholds that call for the application of registration techniques. Relatively to the dual-blood supply, this feature is increasingly considered in liver pharmacokinetic modeling ([28],[38],[36]).

Despite pharmacokinetic approaches normally using continuous dynamic acquisition techniques, in this work the pharmacokinetic model developed was applied to multiphasic image sets, which are characterized by a lower temporal resolution.

2.2   Liver: Morphology and Vascularization

The information concerning liver structure and vascularization has to be taken into account if one wishes to fully understand the way a contrast agent distributes in this organ. The following description considers an extracellular contrast agent.

The blood that enters the liver has two distinct sources: the hepatic portal vein and the hepatic artery. The term portal reflects the purpose of this vessel: hepatic portal vein connects two capillary networks, receiving blood from the capillaries of digestive organs and delivering it to liver capillary-like structures called sinusoids. The portal blood is rich in substances absorbed from the gastrointestinal tract that need to be filtered before entering the systemic circulation.

Besides, liver cells need an oxygenated blood source to work properly, which is provided by the hepatic artery, a direct branch of the abdominal aorta. After being processed by the liver, the blood is then collected by the hepatic vein that directs it to the inferior vena cava, where it will re-enter the heart.

Internal Anatomy of Liver
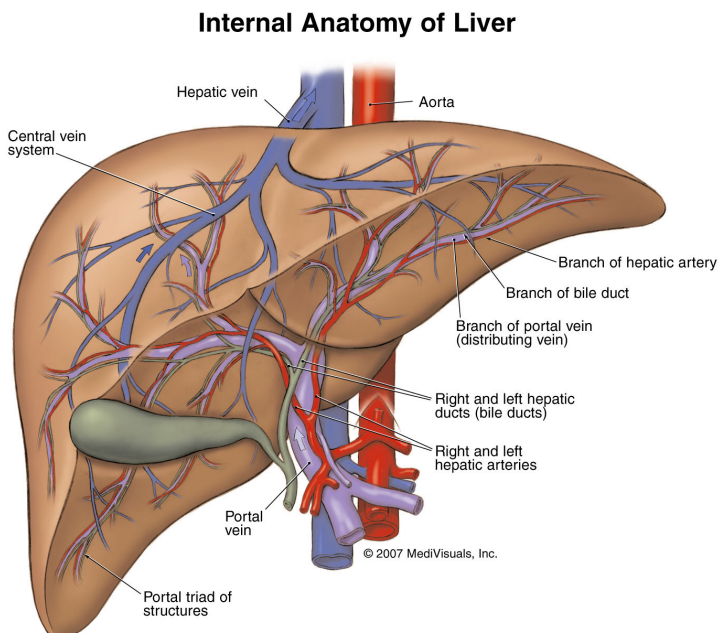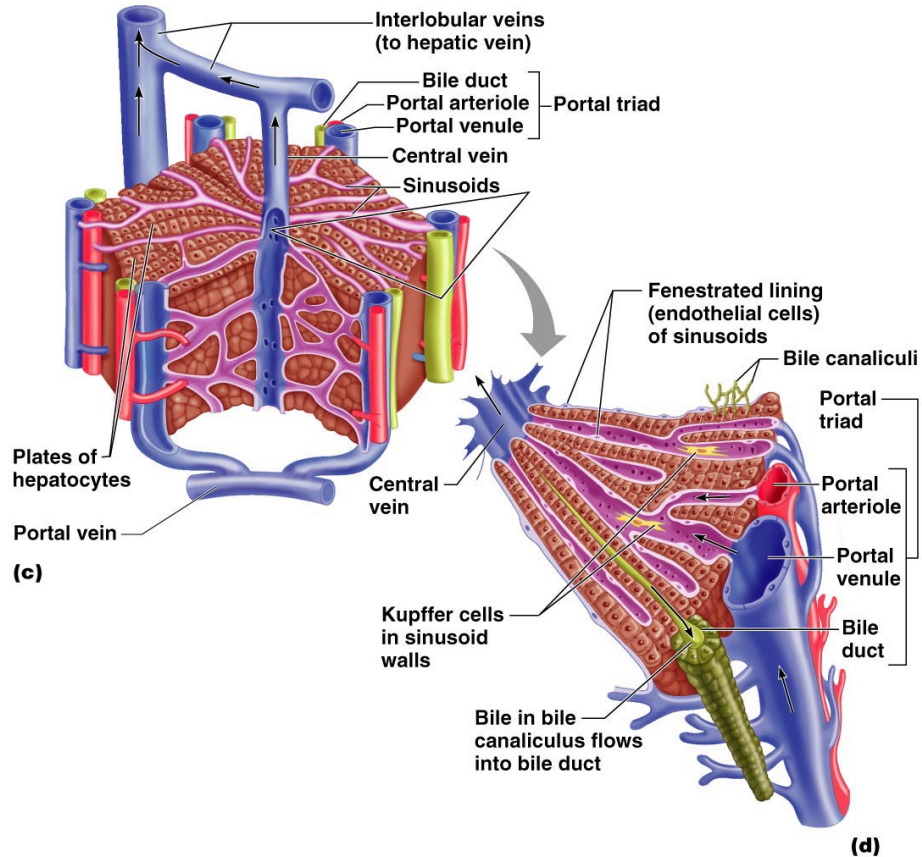
Figure 2.2: Liver representation highlighting its vasculature.

The liver is composed by two lobes: the right lobe and the left lobe. Each one of these is formed by different functional units called lobules. The lobule cross section has a radial symmetry where we can find a central vein, that collects the filtered blood, and several branches from both the hepatic artery and the hepatic portal vein in its periphery (2.3).

Before reaching the lobule center, the blood mixed from its two sources passes through sinusoidal endothelium-lined spaces where it contacts with the cells responsible for filtering the blood: hepatocytes. Although, this contact is not direct: between the sinosoidal endothelium and hepatocytes we can find the space of Disse. This place is full of blood plasma and, in normal conditions, low-weight contrast agents have access to it.

Based on all this information, one is now able to describe how an extracellular contrast agent diffuses in the human body, and namely in the liver. First, the contrast is injected in a peripheral vein. Then, it will join all the blood that comes from other parts of the body and enters the right heart. Next, the contrast performs the pulmonary circulation and re-enters the heart where it is driven into the aorta by the contraction of the left ventricle. Through the branching of the aorta it will reach the hepatic artery and consequently the liver. At the same time, gadolinium enters the systemic capillaries of the gastrointestinal tract. The respective blood is then gathered by the hepatic portal vein and a

second amount of contrast enters the liver with a certain delay. In the liver, the blood from the two distinct sources is mixed and passes through the sinusoids, where part of the contrast is retained in the space of Disse. After the sinusoids, the blood is collected by the hepatic vein. Finally, this leads it to the inferior vena cava and again reaches the right heart, closing the cycle. In parallel, part of the contrast agent is excreted by the kidneys that, in normal conditions, are able to halve the total amount of contrast present in blood in about 1.5 hours[1].

Figure 2.3: Liver lobules. In this picture one is able to identify the main liver structures where blood passes through.

2.3 Liver Tumors

After a general view of the DCE-MRI imaging technique and a description of how the contrast agent spreads within the body and in the liver, one should now focus on the abnormal situations.

Tumors alter liver perfusion regionally, and even globally in some situations. The way it is altered depends largely on the type of tumor. Therefore, in order to better understand the differences in images obtained for different tumors, one should have a particular overview through the most common tumors that can develop in the liver.

Based on its origin, liver cancer can be classified as primary, when is the result from a abnormal development of one or a group of liver cells, or as secondary, when metastasized from a malignant tumor original from other part of the body.

Since every tumor has its own characteristics depending on the type of cells from which it started developing, liver metastasis can vary a lot.

This section starts by describing the primary benign cases, followed by the malignant cases where one founds the most common primary malignant liver tumor and a brief reference to metastatic tumors.

Benign Tumors

Hepatocellular Adenoma

Hepatic adenomas are more frequently observed in women, what may suggest a hormonal influence in its pathogenesis. Normally present in the right lobe they can reach large dimensions, surpassing 10 cm, and be multiple. These two characteristics, if simultaneously present, increase the risk of malignancy that in normal cases would be low.

When observed through a microscope, hepatocellular adenoma cells show increased glycogen, appearing paler and larger than normal. These tumors show no bile ducts and receive only arterial supply, contrasting with the rest of the liver that is mainly supported by the portal venous supply. Kupffer cells may be present but with remote activity.

Hepatocellular adenomas may be detected accidentally or induce symptoms such as pain, the existence of a palpable mass and circulatory collapse if there is intratumor hemorrhage. Diagnose can be made by ultrasound, CT, MRI and radionuclide scans.

In T1-weighted DCE-MRI images these tumors normally show early hyperintensity in arterial phase and hypointensity in portal and latter phases[30] but may contain hyperintense zones due to hemorrhage or presence of fat.

Focal Nodular Hyperplasia

Focal nodular hyperplasia is the second most common benign tumor. Like hepatocellular adenomas, these are also more frequent in women. These tumors are normally solid masses with fibrous core and stellate projections containing atypical hepatocytes, biliary epithelium, Kupffer cells, and inflammatory cells. These lesions have decreased portal vein supply and are associated with the development of portal hypertension. Detection can be made via helical CT, angiography and MRI but difficultly with ultrasound.

In T1-weighted DCE-MRI they are usually hyperintense and marked by an early arterial enhancement and a rapid loss of contrast(washout), showing increased perfusion. Even though, they maintain hyperintensity in latter phases[30].

Hemangioma

Like the previous two tumors, this one is also more frequent in women. Hemangiomas are the most common benign liver tumor having a prevalence of 0.5 to 7% in general population [47]. They are asymptomatic and therefore they are usually detected by accident. Hemangiomas are basically the result of an abnormal development of blood vessel endothelial cells. In this type of tumor, malignant change does not occur and liver resection is only necessary when mass effects are observed.

In multiphasic T1-weighted DCE-MRI they are normally hyperintense at the arterial phase, maintaining this feature even in latter phases.

Hemangiomas can be misidentified with hepatocellular carcinomas in the early phases but distinction can be usually performed at latter ones, when HCC reveal hypointensity[19]. Nevertheless, large cavernous hemangiomas can show a central hypointense region resultant from fibrosis.

Nodular Regenerative Hyperplasia

Nodular Regenerative Hyperplasia consists of multiple hepatic nodules formed as a result of periportal hepatocyte regeneration accompanied with atrophy of surrounding tissue. Its pathogenesis is unknown but studies show that it may be related with abnormalities in the hepatic blood[40], being formed as the response to atrophy of the liver, caused by vascular obstruction of small portal veins or hepatic arteries[39]. The most common symptom in non-cirrhotic liver is portal hypertension and, in some cases, anomalous liver function with progressive symptoms are observed[10].

T1-weighted DCE-MRI images reveal homogeneous hyperintensity in all phases[30].

Malignant Tumors

Hepatocellular Carcinoma

Normally, in the context of liver cancer, studies refer mainly to Hepatocellular Carcinoma (HCC) as it is by far the most common malignant primary liver tumor.

HCC is more common in men and usually arises in a cirrhotic liver. Cirrhosis may be an important contributor to HCC although not being an essential precondition.

Concerning its pathogenesis one may point viral infection by hepatitis B and C, chronical alcoholism, hereditary hemochromatosis and food contamination. In patients with underlying cirrhosis these tumors may be difficult to diagnose since symptoms caused by HCC may be interpreted as a progression of the underlying disease. Nevertheless, the most common symptoms are abdominal pain and the presence of an abdominal mass in the right upper quadrant. Moreover, HCC tumors frequently cause intrahepatic portal vein obstruction [12].

While the hepatocarcinoma tumor grows and perfusion needs are increased, angiogenesis is promoted. This causes new branches from the hepatic artery to form in order to provide more nutrients and oxygen to the cancerous tissue. However, the precancerous nodules - adenomatous hyperplasia - are mostly supplied by the portal vein. Consequently, as the nodule develops into HCC, it may present an outer venously supported region([12],[31]). Nevertheless, mature HCC tumors are mostly supplied by arteries([49],[32]).

Diagnose may be performed using ultrasound, CT, MRI, hepatic artery angiography and technetium scans. Ultrasound may be more appropriate for screening since it is less expensive and is able to identify tumors greater than 3 cm. Besides this, CT and MRI scans have higher sensitivities. When its presence is suspected, a percutaneous liver biopsy of a part of the region detected can be diagnostic. Although, this procedure should be performed with extreme caution since HCC are extremely vascularized.

Patients with Hepatocarcinoma are usually classified according to tumor severity and corresponding life expectancy. In 2001, a study performed by the Liver Cancer Study Group of the University of Toronto[24] compared CLIP[34] (Cancer of the Liver Italian Program) and Okuda staging systems, concluding that CLIP criteria was easier to implement and also more accurate. This classification system is resumed in tables 2.1 and 2.2.

In certain cases therapy may prolong life but surgical resection is the only method for cure. However, factors like underlying cirrhosis, involvement of both hepatic lobes, metastases in other parts of the body and the reduced life expectancy make difficult to find patients with resectable tumors at the time of detection. Therefore, as already mentioned, screening may be essential to increase survival of HCC patients.

Another alternative to be considered is liver transplantation. This shows the same survival after transplantation for patients with a single lesion of no more than 5 cm, or 3 or less lesions with maximum of 3 cm, than for patients with nonmalignant liver disease.

Variables	Scores		
	0	1	2
Child-Pugh stage	A	B	C
Tumor morphology	uninodular and extension ≤50%	multinodular and extension ≤50%	massive or extension >50%
AFP(ng/dL)	<400	≥400	
Portal vein thrombosis	no	yes	

Table 2.1: Cancer of the Liver Italian Program (CLIP) classification system of Hepatocellular Carcinomas[34], where Child-Pugh[42] is another classification system used to assess the prognosis of chronic liver disease, mainly in cirrhosis, and AFP is the concentration of alpha-fetoprotein that, if elevated, may indicate liver cancer. The final classification is obtained adding the scores obtained in each variable. See table 2.2

Final Score	Median survival (months)	Interquartile Range (months)
0	42.5	37.5 - not measurable
1	32.0	25.5 - 38.0
2	16.5	14 - 19.5
3	4.5	4 - 5
4	2.5	1.5 - 3.5
5+6	1.0	1 - 1

Table 2.2: Results obtained in [34] relating scores calculated with CLIP staging system (table 2.1) and median survival in months. The superior limit of the interquartile range for 0 score was not measurable since this group contained several survivors. The results were based in 435 patients with HCC.

Metastic Tumors

Metastasis to liver is very common being found in 30% to 50% of patients dying due to cancer. Symptoms are normally referable only to the primary tumor. Diagnosis can be performed using ultrasound, CT or MRI. Response to all forms of treatment is normally poor and palliation may be the only measure to take.

In T1-weighted MRI, liver metastasis show always hypointensity in latter phases and frequently are hyperintense in arterial phases[30]. Liver metastasis are mainly supplied by the hepatic artery[49].

2.4 Liver Perfusion Analysis

As stated previously, liver perfusion is affected differently depending on the type of tumor. Therefore, in order to classify tumors based on DCE-MRI images, one should be able to assess perfusion characteristics. This can be done by transporting the information contained in the image-level to a perfusion model capable of describing the intensity changes observed. As a result of this operation, a set of parameters, resulting from fitting the model developed to the image data measured, is obtained. Consequently, this approach relies on the capability of the method to describe the processes that underlie the temporal intensity changes in MRI images.

Moreover, when working with low temporal resolution images, applying a model allows fighting the lack of information by adding data derived from the knowledge of the problem being studied. This is done, for example, by establishing relations between observed objects or by limiting the data to physical possible values.

In 1997, Paul S. Tofts wrote a review[50] about the tracer kinetic models used at the time. As he reports, when Gd-DTPA, a Gadolinium-based low-weight contrast agent, also known as Magnevist, started to be used with MRI in the mid-1980s, there was no pharmokinetic or physiologic modeling of the data. This new imaging technique emerged with the purpose of assessing brain tumors and led to the sprout of new 4-D information that lack standard analysis tools.

A few years later, as a response to this problem, three models were presented by three distinct teams: Tofts and Kermode[52], Larsson *et al.*[23] and Brix *et al.*([6],[5]). Tofts describes the different methods and exposes the similarities and differences between them. In parallel it is expressed the need to define standard approaches and nomenclatures to deal with this new problem so that information can be more easily compared between different investigation teams. As a result, in 1999 he, the authors of the described methods and several other investigators published a paper[51] proposing a new standard approach to modelate low-weight tracer kinetics. This document stands today as a reference for all the work developed in this area.
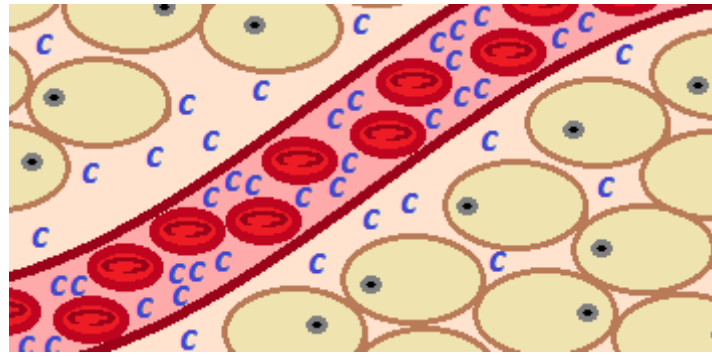

Figure 2.4: Figure showing the contrast (C) in the blood plasma and in the Extracellular Extravascular Space (EES).

Before proceeding further, the main assumptions made by the models presented should be described[50]:
- From this point forward it is assumed that the contrast we are dealing with is an extracellular one. Therefore one considers that it can only be found either inside vessels, diluted in the blood plasma, or outside them, in the extracellular space.
- The term *Extracellular Extravascular Space (EES)* refers to the space outside cells and vessels, excluding the blood plasma, where tracer can be found.
- The pharmacokinetic models consider the *compartment* notion to refer to spaces with homogeneous diffusion properties, where the contrast or the substance in analysis can be found in a uniform concentration.
- The kinetic parameters are considered constant during the time of acquisition.
- The flux between compartments is proportional to the corresponding difference in concentration.

The generalized kinetic model, presented in [51] for the variation of contrast concentration in tissue, dC_t/dt, is:

$$\frac{dC_t}{dt} = K^{trans}C_p - k_{ep}C_t \tag{2.1}$$

, where C_p and C_t are respectively the tracer concentrations in blood plasma and in tissue, K^{trans} is the volume transfer constant between blood plasma and the EES and k_{ep} is the rate constant between EES and blood plasma. It should be noticed that the volume of EES per unit volume of tissue v_e is given by:

$$v_e = \frac{K^{trans}}{k_{ep}} \tag{2.2}$$

The solution of the differential equation 2.1, considering that initially C_p and C_t are 0, is then:

$$C_t(t) = K^{trans} \int\limits_0^t C_p(\tau)e^{-k_{ep}(t-\tau)}d\tau \qquad (2.3)$$

, and the corresponding impulse response:

$$h(t) = K^{trans}e^{-k_{ep}t} \qquad (2.4)$$

, where the impulse corresponds to a pulse of concentration equal to $1/(pulseduration)$.

A few years later, in 2002, a paper describing a method for quantification of hepatic perfusion with dynamic MRI by Materne *et al.*[28] was published. This seems to be the first dual-input model described that takes into account liver dual-blood supply. The model considers the whole liver including capillaries, EES and cells as a single compartment.

The equation that describes the model is then:

$$\frac{dC_L}{dt} = k_{1a}C_a(t) + k_{1p}C_p(t) - k_2C_L(t) \qquad (2.5)$$

, being C_L,C_a and C_p respectively the contrast concentrations in the liver, aorta and portal vein; and k_{1a} the aortic inflow rate constant, k_{1p} the portal inflow rate constant and k_2 the outflow rate constant.

Considering initial null liver concentration and two delay parameters τ_a and τ_p that represent respectively the transit time between the aorta and the portal vein, and the the liver, we obtain:

$$C_L(t) = \int\limits_0^t \left[k_{1a}C_a(t' - \tau_a) + k_{1p}C_p(t' - \tau_p) \right] e^{-k_2(t-t')}dt' \qquad (2.6)$$

The method was validated *in vivo* in nine male rabbits with normal liver function. Liver perfusion parameter measurements were made before DCE-MRI acquisition using radiolabeled microspheres. The results obtained are found in table 2.3.

Property	Microspheres $(mLmin^{-1}100g^{-1})$	DCE-MRI $(mLmin^{-1}100g^{-1})$
Hepatic flow	93 ± 42	100 ± 35
Arterial flow	20 ± 10	23 ± 13
Portal flow	73 ± 35	84 ± 32

Table 2.3: Results obtained in [28] for *in vivo* validation of the assessment of hepatic perfusion using DCE-MRI images.

Three years before (1999), Scharf *et al.* [45] performed similar experiments demonstrating the potential of DCE-MRI to assess hepatic perfusion. The experience described had also the objective of testing the ability of DCE-MRI to measure liver perfusion. Therefore, DCE-MRI was performed in nine pigs before and after partial portal occlusion. In parallel, perfusion was measured using thermal diffusion probes.

The results from DCE-MRI images perfusion analysis of the average portal flow had a correlation of r=0.93 with the results obtained with thermal diffusion probes. Acquisition was T1-weighted, performed using a 1.0 Tesla MRI scanner and high temporal resolution was used, having been acquired 120 images over 4 minutes from one section. A linear relation between intensity and Gd concentration was considered and perfusion curves were obtained using a linear dual-compartment model with single input.

Besides the relevance of the results shown, the model suffered from considering only one input function. Moreover, both in these and in the experiments performed by Materne *et al.*, the signal used corresponds to the whole liver, which would make impossible tumor classification.

In 2005, a review from Pandharipande *et al.*[38] on Perfusion Imaging of the Liver was published. According to the authors "The ability to resolve hepatic arterial and portal venous components of blood flow on a global and regional basis constitutes the primary goal of liver perfusion imaging." The paper described the development of HCC from dysplastic nodules with focus on the consequent arterial fraction increase.

Moreover, the increased hepatic arterial liver perfusion, in a local and global basis, is also referenced in metastic disease. Analysis of the balance between arterial and venous perfusion is also reported as a possible strategy to diagnose cirrhosis. The review concludes highlighting the importance of DCE-MRI as a non-invasive diagnostic tool and pointing the importance of increasing temporal and spatial resolution in this imaging technique.

A different approach to model liver perfusion was proposed by Mescam *et al.* [29] in 2007. The method presented a very interesting and complete perfusion model, describing carefully hepatic perfusion. Although the elevate number of variables may pose difficulties in terms of its application to tumor classification.

Recently, in 2009, Matthew Orton *et al.* described a dual-input single compartment pharmacokinetic model of liver perfusion[36]. As they state, spatial resolution of MR and CT studies are sufficient to allow dual-input single-compartment modeling viable, especially if the data is acquired at a high temporal resolution. As a result, arterial and portal perfusion can be analyzed separately and its ratio assessed. As Pandharipande *et al.*, the authors refer to metastasis and cirrhosis liver perfusion affection, highlighting the value of liver arterial ratio assessment in the diagnose of this diseases. The model presented takes into account that the blood that comes from the two distinct sources mixes together at liver sinusoids (figure 2.3).

Consequently, the input function is given by the weighted sum of the portal and arterial input functions:

$$C_p(t) = \gamma C_A(t) + (1 - \gamma)C_V(t) \tag{2.7}$$

, where C_p is the mixed blood plasma contrast concentration, C_A is the arterial blood plasma contrast concentration, C_P the portal blood plasma contrast concentration and γ the arterial ratio.

Considering this, the contrast leakage from hepatic sinusoids to the EES is then modeled. This is done using the generalized kinetic model defined by Tofts *et al.* in 1999. A delay τ is introduced to represent the time taken by the blood from the vessels where the input functions signal was measured to the liver sinusoids.

Thus, the model is mathematically expressed by:

$$C_t(t) = K^{trans}C_p(t) \otimes e^{-k_{ep}(t-\tau)} \tag{2.8}$$

, where the impulse response form was used and C_t represents the contrast concentration in tissue.

The model is similar to the one from Materne *et al.*, with $k_{1a} = \gamma K^{trans}$ and $k_{1p} = (1 - \gamma)K^{trans}$.

According to another publication of the same authors[35], the input functions can be modeled considering that the concentration in blood plasma is the superposition of the bolus shape and its shape after modification by the body impulse response:

$$C_{input}(t) = C_B(t) + C_B(t) \otimes G(t) \tag{2.9}$$

, being $C_B(t)$ the bolus function and $G(t)$ the body impulse response.

If we now consider a bolus of the form:

$$C_B(t) = \begin{cases} 0 & \text{if t=0} \\ a_B t e^{-\mu_B t} & \text{if t>0} \end{cases} \tag{2.10}$$
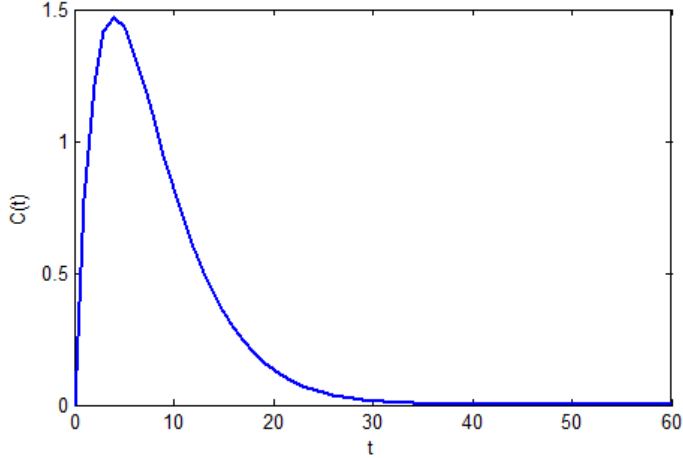
Figure 2.5: Bolus model function described in equation 2.10 with $a_B = 1$ and $\mu_B = 0.25$.

, and a body impulse response $G(t) = a_G e^{-\mu_G t}$, we obtain the following input model function:

$$C_{input}(t) = A_B t e^{-\mu_B t} + A_G (e^{-\mu_G t} - e^{-\mu_B t}) \qquad (2.11)$$

, with $A_B = a_B - a_B a_G / (\mu_B - \mu_G)$ and $A_G = a_B a_G / (\mu_B - \mu_G)$.

The small number of variables included in this liver perfusion model turns it adequate to a data fitting approach.

2.5   Registration

The assessment of the perfusion curves based on images is only possible when we are able to follow the intensity variation of a determined region through time. Therefore, every image from each study should be aligned such that each voxel corresponds always to the same region, or more specifically, to the same group of cells.

Besides being easy to understand the problem, alignment of abdominal DCE-MRI images is a very challenging task.

One can distinguish three main factors in this particular type of medical image that explain the difficulty of this alignment. Firstly, the lack of an intensity fixed meaning in MR images jeopardize the direct intensity comparison even for two images of the same body region, acquired in the same scanner, with the same protocol[33]. Secondly, tissues differential contrast uptake alters image in a very heterogenic way. Last but not least, abdomen has a great freedom of movements and breathing, peristalsis and other factors may cause organs to deform and change their relative position inside the abdominal cavity. These changes combined altogether make almost impossible a perfect alignment.

In order to address these issues, inter-modality similarity measures that can overcome non-linear intensity variations are used. Also, in order to minimize motion artifacts, patients may take medication to reduce peristalsis[27], images may be acquired in breathold, like the ones used in this thesis, some scanners use cardiac-triggered acquisition and constant progress is made towards faster MR acquisition.

In this work, image alignment was performed by means of a very flexible registration software: drop registration toolkit([16],[21]). This tool considers Free Form Deformations (FFD)[44] and proposes a solution based on Markov Random Field(MRF) Optimization. The interest in FFD comes from the degree of flexibility provided by this type of transformation but also because these allow diminishing considerably the dimension of the problem and provide smooth results.

In a very simple way, FFD consider a deformable grid superimposed onto the image one seeks to deform. In this grid the interaction is made through the intersection points of the grid, referred to as the control points.

After moving one of these points, the pixels of the deformable image will deform according to its distance to the displaced control point and the overall image will be reconstructed using interpolation techniques. Based on this concept, drop seeks to find the group of displacements that, once applied to each point of this deformable grid, will maximize the similarity between the corresponding deformed image and the reference image. This is done considering the group of control point deformations as a set of random variables respecting the MRF properties - MRF Optimization[21]. The concept of FFD can be better understood in image 2.6
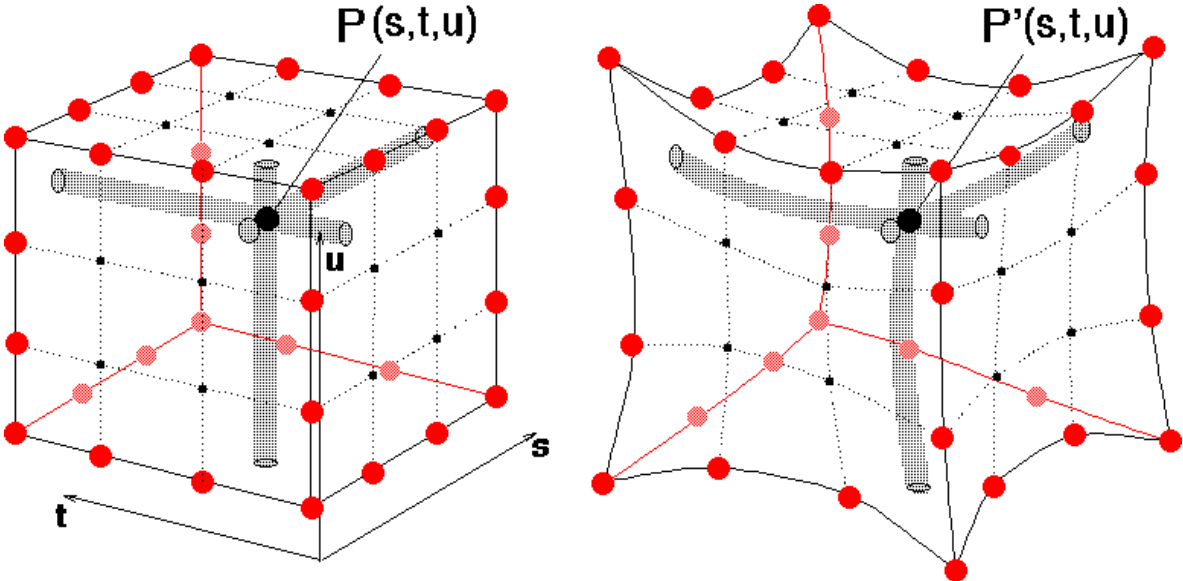

Figure 2.6: Free Form Deformations[56].

The alignment process or registration can be seen as the problem of finding the transform $T(x)$ such that:

$$\forall x \in \Omega, I_t(x) = h \circ I_d(T(x)) \tag{2.12}$$

, where I_t is the target image; I_d is the deformable image; h is a non-linear operator that explains the changes between images related to evolution of the low-weight contrast agent in blood vessels and EES, and also imaging artifacts; T is the coordinate transform and x is the coordinate vector.

Now, let us consider a deformation grid $G : [1, L_1] \times [1, L_2] \times [1, L_3]$, with $L_1 \times L_2 \times L_3$ control points, superimposed onto the two images to be aligned: $I_d, I_t : [1, N_1] \times [1, N_2] \times [1, N_3]$, such that the deformations in the grid will only affect the deformable image. Thus, the transformation within a point x of I_d will be given by:

$$T(x) = x + D(x) \tag{2.13}$$

, with

$$D(x) = \sum_{p \in G} \eta(|x - p|)d_p \tag{2.14}$$

17

,being d_p the displacement vector corresponding to p; and η a weighting function that expresses the contribution of the control point p to the deformation in the point x.

Drop allows choosing different interpolation techniques to perform the Free Form Deformations. In this work B-Splines were used, and consequently $D(x)$ becomes

$$D(x) = \sum_{l=0}^{3} \sum_{m=0}^{3} \sum_{n=0}^{3} B_l(u) B_m(v) B_n(w) d_{i+l, j+m, k+n} \tag{2.15}$$

, where $i = \lfloor x/\delta_x \rfloor - 1$, $j = \lfloor y/\delta_y \rfloor - 1$, $k = \lfloor z/\delta_z \rfloor - 1$, $u = x/\delta_x - \lfloor x/\delta_x \rfloor$, $v = y/\delta_y - \lfloor y/\delta_y \rfloor$, $w = z/\delta_z - \lfloor z/\delta_z \rfloor$, B_l is the B-Spline lth basis function, and $\delta_x = \frac{N_1}{L_1-1}$, $\delta_y = \frac{N_2}{L_2-1}$, $\delta_z = \frac{N_3}{L_3-1}$ the control point spacing.

In order to direct the evolution of the deformations in each control point, information concerning the alignment of the image has to be assessed. The relevance of each voxel in the direction of the deformation of a determined control point will obviously depend on their mutual distance. Drop uses different weighting techniques to answer this problem depending on the similarity measure used. When using Mutual Information[26], a simple mask centered on the control point with certain dimensions is applied. Consequently, the deformation in one control point depends on the voxels selected by this mask. Since MI is a statistical measure, the similarity value that reaches each control point is computed based using this neighbor voxels. Given that the size of this mask depends on the resolution of the grid, increasing resolution decreases the amount of data that each control point has access when making the decision of the deformation direction. According to the authors of drop[16], this effect does not play a crucial role and very good results are shown using statistical measures. Nevertheless, it should be taken into account when choosing the grid resolution and, obviously, the number of bins used in the MI computation.

Returning to the formulation of the registration problem, the energy function one pretends to minimize in order to align I_d and I_t has the following form:

$$E = E_{data} + \lambda E_{smooth} \tag{2.16}$$

, where one finds two distinct terms: the data energy term that reflects the similarity measured value between I_d and I_t and the smoothness term with variable weight λ that allows controlling the smoothness of the result obtained. The first term is the sum of the similarity measure calculated for each control point,

$$E_{data} = \sum_{p \in G} MI(M_p \otimes I_t(x), M_p \otimes I_d(T(x))) \tag{2.17}$$

, being M_p the mask centered in p with predefined dimensions that selects its neighborhood. Relatively to the smoothness term, this should penalize displacement differences between close grid points. Therefore is given by:

$$E_{smooth} = \sum_{p \in G} \sum_{q \in N(p)} |d_p - d_q| \tag{2.18}$$

, where $N(p)$ is the neighborhood of the control point p.

The final solution is found by an iterative process using MRF optimization based on linear programming. As already referred, the registration algorithm will seek the group of displacements that minimize the energy function described.

2.6 Imaging Studies used in this Thesis

The work developed in this thesis used multiphasic T1-weighted DCE-MRI images with 6 timepoints each. The first timepoint corresponds to the non-contrast acquisition, the following three to the arterial

phase acquired using keyhole, the fifth one to the portal phase and the last one to the equilibrium phase.
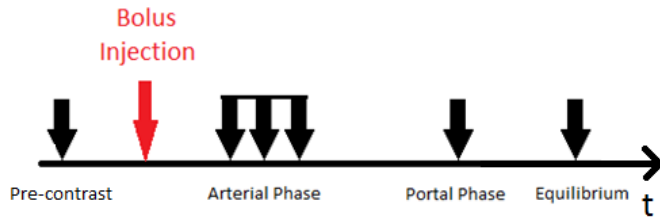

Figure 2.7: Schematic representation of the different phases and corresponding acquisitions through time.

The history of events that underlie the acquisition process may be reported as follows:

- First, a simple MRI acquisition is performed without any contrast. Two images may be acquired in order to ensure the quality of the scan performed.
- Then, the contrast - Gadovist with a Gadolinium concentration of 1.0 M- is injected at a constant speed of 1.5 ml/s. The total amount of contrast injected depends on the patient's body weight, being 0.1 mmol of Gd per each kg of body weight.
- Immediately afterwards, 15 to 20 ml of normal saline are injected at the same speed with the purpose of maintaining the coherency of the bolus.
- After contrast injection, the heart and surrounding vessels are tracked at a constant frequency of 2 images per second.
- The moment the contrast is detected in the left heart or in the aorta, the patient is told to sustain its breath and the arterial phase is launched.
- In the arterial phase the k-space is acquired partially, according to the keyhole technique. As so, in the first two images of this phase only the low frequencies are registered, followed by the third image which corresponds to the complete acquisition. The whole phase lasts 21 seconds, taking the initial images 3.5 s and the last one 14 s.
- After this breathold acquisition, the patient is allowed to breath for about 10 to 20 seconds.
- Then, the patient returns to sustain its breath and the portal phase is acquired.
- The process ends with another free-breathing interval followed by the last acquisition - equilibrium phase.
- Apart from the arterial phase images, each one of the others takes about 20 seconds to be acquired.

From this description we should conclude that the time course of each case may vary considerably. This depends mostly on patients ability to sustain their breath, influencing the free-breathing intervals, but also on its blood flow and corresponding speed, which affect the time between the contrast injection and the start of the arterial phase.

The cases analyzed are summarized in table 2.4.

All imaging studies were acquired with a 1.5 Tesla superconducting magnet (Philips Achieva; Hospital Erasme, Brussels) with the patients placed in the supine position. A T1-weighted Gradient Echo sequence was used with a flip angle of 10º, repetition time of 3.93 msec and echo time of 1.87 msec.

In terms of fat suppression, Spectral Adiabatic Inversion Recovery (SPAIR) was used.

Each image has the following matrix dimensions: 256x256x150 with a corresponding pixel spacing of 1.75 mm and a slice thickness of 3.6 mm with spacing between slices of 1.8 mm.

Patient	Pathology	Tumors analyzed	Time Vector (s)
1	Neuro-endocrine metastase	1	$\{0, 54, 58, 61, 117, 146\}$
2	Nodular Regenerative Hyperplasia	2	$\{0, 70, 75, 80, 191, 238\}$
3	Focal Nodular Hyperplasia	1	$\{0, 64, 67, 71, 156, 188\}$
4	Hemangioma	1	$\{0, 63, 66, 70, 119, 165\}$
5	Hepatocellular Carcinoma	3	$\{0, 56, 59, 63, 124, 158\}$
6	Hepatocellular Carcinoma	1	$\{0, 55, 59, 63, 164, 199\}$

Table 2.4: List of patients corresponding to the images used in this thesis.

Chapter 3

Model

This work had as initial data the DCE-MRI images with confirmed diagnosis given by the Hospital Erasme, Brussels. Based on these, it was intended to develop a classification method that could assess perfusion differences between malignant and benign tumors.

This problem had already been studied at ISR by Caldeira, L.; Silva, I. and Sanches, J. ([9],[7],[8]), having been shown some differences between wash-in and wash-out rates from benign and malign lesions. Although the method used revealed interesting results, it considered only a single input function, omitting liver characteristic dual-blood supply. Despite this, it demonstrated how perfusion parameters can be accessed through the analysis of voxel-by-voxel tumor perfusion curves.

Many studies and reviews ([28],[50],[18],[13],[36],[35],[43],[25],[37], and many others) point in the same direction, revealing that pharmokinetic analysis has a wide range of potential applications related to tumor analysis. Thus, a similar approach was made to address the liver tumor classification problem.
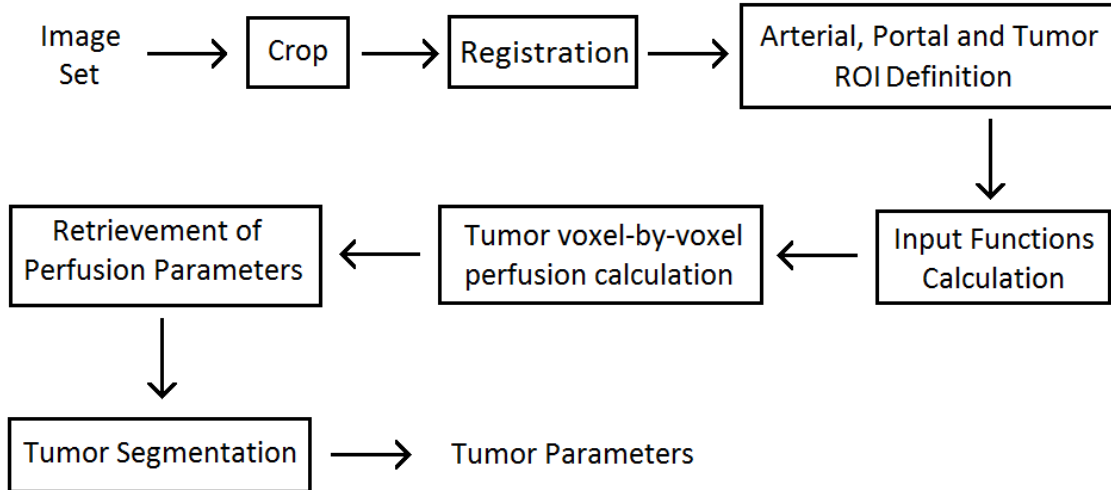
Figure 3.1: Schematic representation of the algorithm different processes underlying the tumor parameter accessment.

The strategy used is described as follows. First, a region containing the whole liver is simply extracted by cutting the initial images. One should consider that DICOM files of distinct images may

21

contain differences in the intensity scales that need to be corrected. Then, since it is pretended to make a voxel-by-voxel pharmacokinetic analysis, one should align the images of each study.

After the alignment, the perfusion model may be applied and the corresponding parameters extracted. However, this task needs a previous definition of the regions from where the input functions signal will be measured, as of the volume where the analysis will be made. In a normal procedure the tumor should be found at the center of this Volume Of Interest (VOI).

Having the analysis been completed, the task of defining the spatial limits of the tumor presents easier than before. A simple segmentation technique based on the Region Growing algorithm is then applied. The tumor perfusion data can now be retrieved and the mean values and standard variation of its parameters are calculated.

Finally, results from different tumors are compared. The algorithm described is schematically presented in figure 3.1.

Next, each part of the algorithm is described in more detail.

3.1   Crop

The images acquired contain a lot of unusefull data that makes heavier image processing. Taking into account the purpose of this work and the information needed to apply the analysis method, we should conclude that a box containing the whole liver, a part of the aorta and obviously the portal vein is sufficient. Therefore, the crop reveals to be a very simple task that only needs the identification of the limits of the structures described.
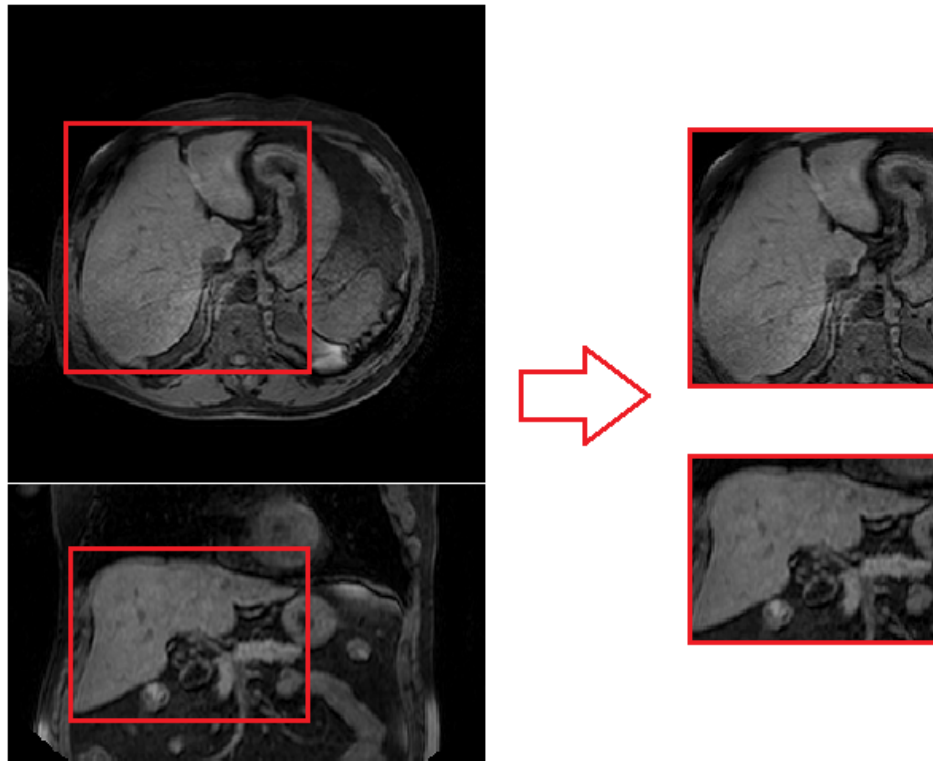

Figure 3.2: Example of the liver crop.

3.2   Registration

As already mentioned, the image alignment was accomplished using drop registration tool. This tool is not directed specifically to DCE-MRI images, having been developed with the purpose of being able to respond to a broad group of registration problems. Consequently, the user should take several options in terms of the registration parameters.

As previously mentioned, the intensity variation caused by the diffusion of the contrast in the human body, turns impossible the establishment of intensity identity relations between voxels of the two different images from the same study. This problem is resolved by applying statistical similarity measures such as the Mutual Information (MI) or its normalized version (NMI).

The similarity measures are defined as follows:

$$MI(I_A, I_B) = H(I_A) + H(I_B) - H(I_A, I_B) \tag{3.1}$$

, where $H(\cdot)$ is the entropy, given by:

$$H(I) = -\sum_i p_I(i) \cdot log(p_I(i)) \tag{3.2}$$

, being $p_I(i)$ the probability of observing a voxel with intensity i in the image I. $H(\cdot, \cdot)$ is the joint entropy of two images which is given by:

$$H(I_A, I_B) = -\sum_{i,j} p_{I_A I_B}(i,j) \cdot log(p_{I_A I_B}(i,j)) \tag{3.3}$$

, where $p_{I_A I_B}(i,j)$ is the probability of observing one voxel with intensity i in the image I_A and intensity j in the image I_B.

The normalized version of mutual information, also referred as Entropy Correlation Coefficient, is simply:

$$NMI(I_A, I_B) = \frac{H(I_A) + H(I_B) - H(I_A, I_B)}{H(I_A) + H(I_B)} \tag{3.4}$$
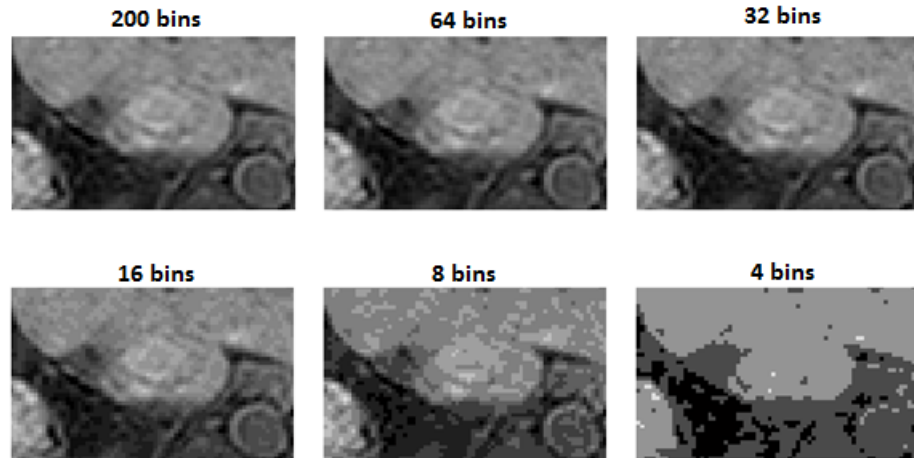

Figure 3.3: Perspective of how the number of bins affect the image and the ability to distinguish objects in it.

In order to calculate the probability values, the intensity scale has to be divided in a certain number of equal intervals or bins. The number of bins has also to be optimized. In the one hand, the greater its value the more sensible to noise the similarity measure will be. On the other hand, a value too small does not allow to distinguish objects in the image, turning impossible the alignment task (see figure 3.3).

One should consider that drop calculates MI and NMI in a local area around the control point whose dimensions depend on the size of the grid. Besides, since it is being developed a voxel-by-voxel analysis, the grid resolution has to be fine enough to allow obtaining the level of accuracy needed. Consequently, an elevate number of bins may turn the calculation unstable since a small amount of voxels are used to compute MI and NMI.

To decide about the similarity measure to use, as the corresponding number of bins, 60 registration tests were performed. The results obtained can be found in figure 3.4.
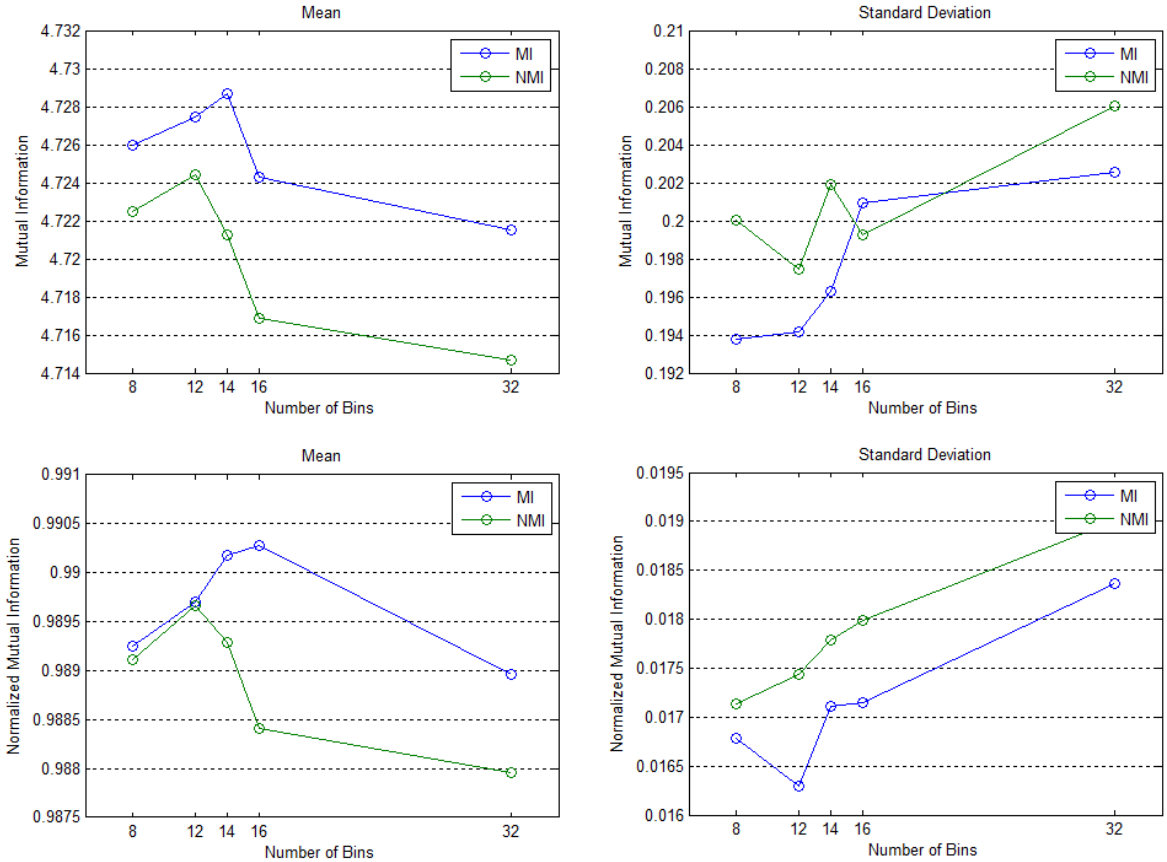

Figure 3.4: Registration tests where two similarity measures were tested with 4 different number of bins. The quality of the results is measured using the two similarity measures and mean values and standard deviation is presented. The results were based in 60 image alignments. The 6 alignments of each point correspond to the application of two different tests in 3 image studies: similar images test, where two images without contrast are aligned; and opposite images test, where a pre-contrast image is aligned with the one in the equilibrium phase. The values of MI and NMI used to evaluate the performance of the alignments where calculated using 256 bins. The calculation was performed excluding the peripheral voxels that, due to the image transformation, had no information.

A brief look at the results allows concluding that using Mutual Information as similarity measure

with 14 bins proves to be the best solution. It is also noticed the instability phenomenon referred previously by means of the standard deviation increase with the number of bins.

In terms of the grid, drop uses a hierarchical approach, being the registration performed in several levels. As so, it starts with a large grid and, after the alignment process having been finished in each level, the size of the grid is reduced to a half of the former one.

Since the displacements amplitude is connected to the size of the grid, the rigid body deformations are normally corrected in the first level. The default value of levels is three, value that the drop authors suggested as being adequate for the most part of alignment problems. Accordingly, this was the value of levels chosen to align the image studies.

The grid resolution was chosen so that the finer grid level had a grid distance of about 8 voxels. Several attempts were made using finer grids but no improvement was noticed.

Finally, the smoothening term weight - λ. This parameter varies considerably between different situations. Normally was considered a λ value of 1, however in images that presented no great deformations a greater value - 10 - was used, taking into account that no great displacements need to be applied and a smooth result is desired.
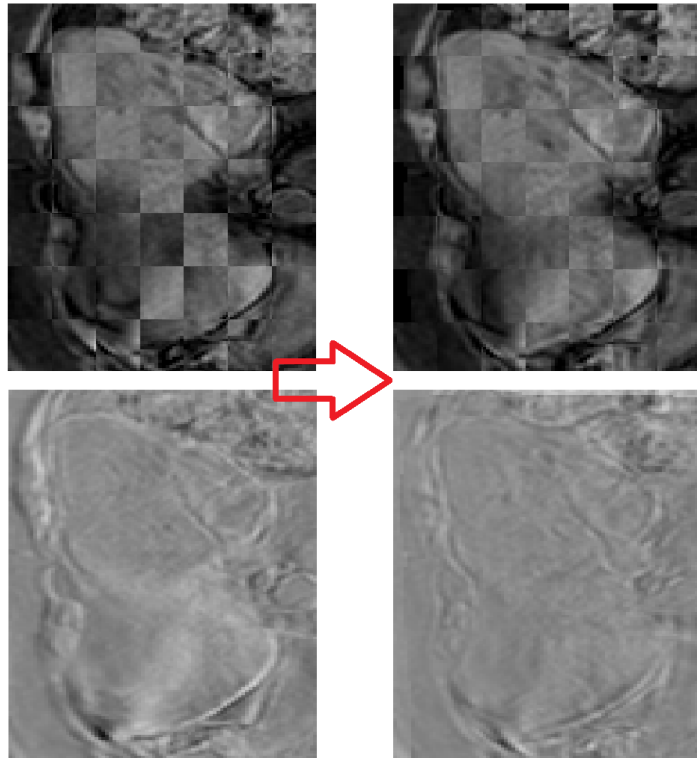
Figure 3.5: Registration example. A checkboard view and the difference between the two images is shown before and after the alignment.

Having now the main parameters chosen, the registration of each study was performed. This was made choosing the same target image for all the alignments of each image study. The choice of anchor image was made considering that the three arterial phase images are already aligned, having been acquired using keyhole and consequently sharing the high frequencies section of the k-space. As a result, the middle arterial phase image was chosen as anchor. Besides reducing the time taken to align each study, one should not forget that interpolation techniques that deteriorate the quality of the image are used, causing a blurring effect. Therefore fewer alignments allow decreasing the number

of images that suffer this negative effects.

An example of a successful alignment is shown in image 3.5.

3.3 ROI definition

As it will be discussed later, the application of the pharmacokinetic model depends on the previous knowledge of the contrast variation in the aorta and in the portal vein. Therefore, it is necessary to define two regions inside each one of these two vessels. This task is performed manually and, considering the purpose of these Regions of Interested, a depth of only one slice proves to be sufficient. However, this is not the case for the tumor VOI since one pretends to analyze the whole tumor and not a single slice of it.

3.4 Perfusion model

Input functions calculation

The main challenge present in this thesis is the lack of information resultant from using low resolution images. In practice, the initial data consists of only 6 intensity values, observed per voxel in different times. First, in order to be able to proceed with a pharmacokinetic analysis, a relation between intensity and contrast concentration should be established. The best way to do this is by previous calibration, filling several tubes with different solutions, with known contrast concentrations, and imaging them [28]. Unfortunately, this information was not known. Even so, some studies point a linear relation between contrast concentration and relaxivity[41]. Considering this, contrast concentration can be approximated by the relative signal, or:

$$C(t,x,y,z) \approx \frac{I(t,x,y,z) - I(0,x,y,z)}{I(0,x,y,z)} \tag{3.5}$$

, where $C(t,x,y,z)$ is the contrast concentration at time t in the voxel with coordinates (x,y,z); and $I(t,x,y,z)$ is the intensity value of the same voxel at the same time.

Accordingly, the relative signal is now calculated for the mean intensities of the aorta and hepatic portal vein selected regions.
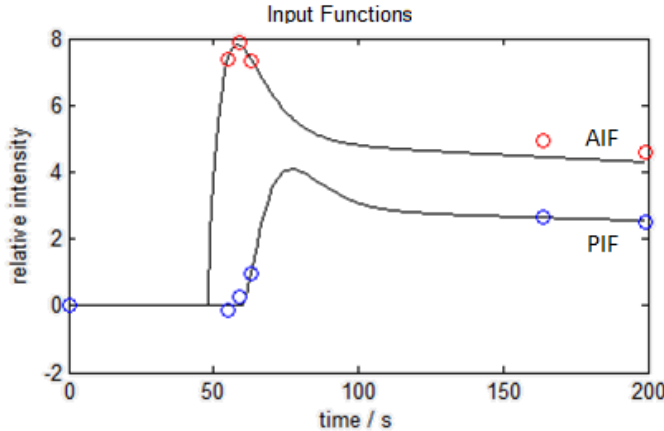

Figure 3.6: Input functions example. The red points correspond to the arterial signal, and the blue ones to the hepatic portal signal.

Having now information concerning the contrast concentration, one should now focus on the determination of the perfusion curves that will be used as input functions. This task begins by fitting the model shown in equation 2.11 to the signal retrieved from the aorta, using a least-squares approach.

Since the contrast present in the portal vein passes before in the aorta, this curve should be obtained considering the arterial function as input. As so, the venous input function may be modulated considering Tofts generalized kinetic model as:

$$\frac{dC_{PIF}(t)}{dt} = K_{AP}^{trans} C_{AIF}(t - \tau_1) - k_P C_{PIF}(t) \tag{3.6}$$

, where K_{AP}^{trans} is related to blood flow between the two regions.

The model can be interpreted as follows: the increase in the amount of contrast that one founds in the hepatic portal vein depends on the contrast concentration in the aorta, a few seconds before, and on the flow existent between these two vessels. In parallel, the higher the concentration in the portal vein, the more this contrast will tend to diffuse into the EES and to the other blood plasma. k_P is then connected to the speed that characterizes this diffusion process. Overall, this may be viewed as an example of what is described by Tofts *et al.* in [51] as a flow limited situation.

In conclusion, the hepatic portal input function is obtained by fitting the following equation:

$$C_{PIF}(t) = K_{AP}^{trans} C_{AIF}(t) \otimes e^{-k_P(t - \tau_1)} \tag{3.7}$$

An example of the arterial and portal input functions obtained is visible in figure 3.6. As one begins to notice, using more points as a basis for the perfusion curves calculation may cause a significant increase in the accuracy of the method.
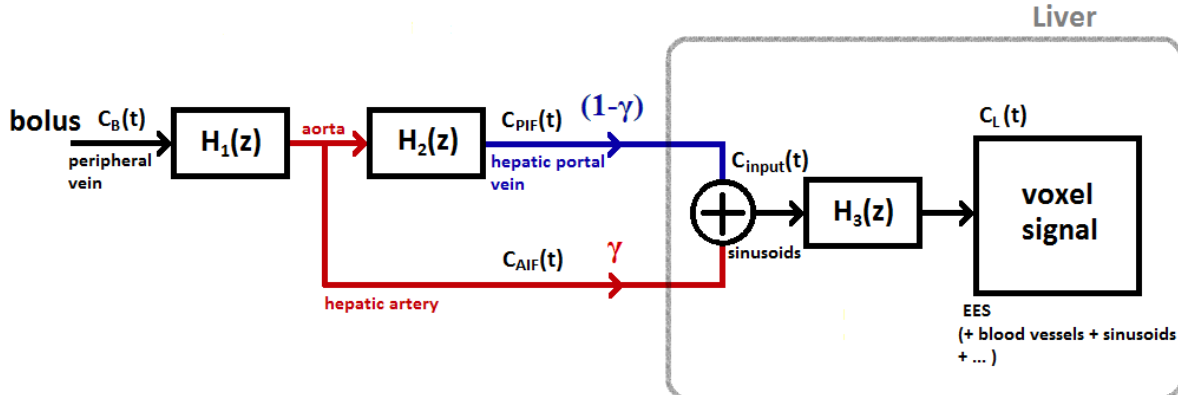

Figure 3.7: Pharmacokinetic model used.

Liver perfusion calculation

Having an approximate measure of the contrast that is entering the liver by the hepatic artery and the hepatic portal vein, one is now able to model liver perfusion. In contrast with the previous situation, in this process the concentration in the liver is limited by the permeability of the sinusoids epithelium, depending on the amount of contrast that flows between the sinusoids and the liver EES. Nevertheless, in the corresponding volume of each acquired voxel one should find, apart from the hepatocytes, other structures such as sinusoids and small vessels. Consequently this is a mixed situation, where the concentration 'observed' is both limited by the input flow and by the EES-to-sinusoids permeability. Nevertheless, besides the perfusion parameters being influenced by different factors, the generalized kinetic model remains unchanged, and can be described as follows:

27

$$\frac{dC_L(t)}{dt} = K_L^{trans} C_{input}(t - \tau_2) - k_L C_{input}(t) \tag{3.8}$$

, or

$$C_L(t) = K_L^{trans} C_{input}(t) \otimes e^{-k_L(t - \tau_2)} \tag{3.9}$$

, where $C_{input}(t)$ is the input concentration, given by:

$$C_{input}(t) = \gamma C_{AIF}(t) + (1 - \gamma) C_{PIF}(t) \tag{3.10}$$

One is now in position to perform the model fitting in each voxel. The model corresponding to the whole perfusion model is schematically represented in figure 3.7.

3.5 Perfusion Parameters

Having calculated the two input functions, the liver perfusion model is applied in each voxel of the tumor ROI using least squares. From this process we obtain a set of perfusion parameters: K_L^{trans}, γ, k_L τ_2, which characterize the voxel perfusion curve. This curve has also several characteristics that may be useful for tumor characterization, such as: Maximum value and the time when it occurs; the perfusion volume, calculated as the integral of the perfusion curve; wash-in rate measured as the maximum derivative before the maximum and wash-out rate measured as the minimum derivative after the maximum value. Here the approach was based on retrieving a considerable amount of parameters in order to use the maximum information possible for the classification. The 9 parameters described are registered for each voxel of the tumor ROI, allowing building several parameter maps.

3.6 Segmentation

The tumor VOI is defined as a 3D box in order to allow the user having the perception of the differences, in terms of parameters values, between the tumor and the surrounding area. However, the tumor voxels have to be identified, so that the mean and standard variation values of the tumor perfusion parameters may be calculated.

Since the perfusion maps may help identifying the tumor limits, this task is performed after fitting the data to the perfusion model. The segmentation applied in this thesis is based on the Region Growing algorithm. This method of segmentation consists of starting with one point that we already recognize as belonging to the structure we want to extract - the seed point -, and systematically adding the neighbors that meet a certain condition of similarity. When analyzing the neighborhood of one voxel, the conditions imposed are:
- the intensity of the neighbor should be between an upper and a lower bound defined by the user;
- the difference between one voxel and its neighbor should be smaller than a predefined limit, which grants a certain homogeneity of the segmented structure.
To define the values corresponding to these conditions the user starts to choose the image where the tumor can be better distinguished from the surrounding tissue. Then, since the tumor ROI should have the tumor in its center, a small centered cube is retrieved from the selected image. After this, the cube mean values and standard deviation are calculated. The segmentation is then performed considering as limits the mean minus α times the standard deviation and the mean plus α times the standard deviation, where α is defined by the user. The maximum intensity difference between one voxel and its neighbor is β times the standard deviation observed in the cube, where β is another user-defined value.

An example of a badly chosen β value and consequent leakage is shown in figure 3.8. In order to avoid this, the search region is limited to the tumor ROI. Moreover, β is chosen small, what may

28

cause several tumor voxels to not be identified by the segmentation algorithm. Consequently, a closing operation is applied to the final segmentated region. As a result, the holes contained in the pre-segmentated region corresponding to the non-identified voxels are filled. More details on this type of morphological operation can be found in [17].

Figure 3.8: Example showing how a large β value can cause leakage. However, interestingly the error consists of a parasite identification of one vessel and an intensively vascularized region that seems to be the spleen. The tumor (Angioma) is the mass found in the left upper corner.

Having concluded the segmentation and consequently identified the tumor voxels, the mean and standard variation of the perfusion parameters corresponding to the tumor are calculated.

Chapter 4

Graphical User Interface

The model presented in the former chapter was implemented in MATLAB, and a Graphical User Interface(GUI) was developed in the same environment. This allows not only connecting all the parts of the algorithm, but also improving the interaction between the imaging data, the algorithm and the user.

The GUI developed here is composed by 3 different windows:

-the main window (figure 4.1);
-the ROI (Regions-of Interest) window (figure 4.2);
-the perfusion window (figure 4.3);

In the first one, the user loads and saves data, performs the tumor segmentation and analyses the results. In the ROI window, the user defines the arterial, portal and tumor regions. The main characteristic found in this component is the ability to view all the images from the image set at the same time. This is of great importance when defining the several ROI, since registration may have not produced the desired result and the user accompanies the region selection process in the complete image set. Finally, in the perfusion window the user has access to the input functions and is able to test the perfusion model. It should be noticed that the model fitting process is performed using the *lsqnonlin*() MATLAB function. In a very general way, this works by starting with a initial set of parameters and converging to the solution that minimizes an user-defined function. In this case the cost-function used is the sum of the squares of the distances between the 6 initial points and the value of the perfusion curve at the corresponding times. The parameters obtained are contained between user-defined bounds. Consequently, the solution depends on the initial guess and the model should be calibrated before applying it to the tumor. The calibration is simply made by performing a pharmokinetic analysis in the normal liver and in the aorta. The values obtained for the arterial ratio will allow assessing the response of the model to two regions whose supply is known. In terms of the liver, every result above 25% is considered wrong and forces a re-definition of the initial parameters of the input functions. Relatively to the aorta, obviously only results close to 100% are accepted.

In order to improve the understanding of how an user performs a normal analysis, a brief step-by-step description follows:

   - First, the user starts by loading the imaging data. The input object should be a *.mat* file containing a 4D matrix with the pre-registered images and the time vector with the acquisition times.
- Then, in the ROIs window, the 3 regions (arterial, portal, tumor) are defined. Initially the '*tumor ROI*' may include only a normal part of the liver in order to calibrate the input functions.
- Now, the program has the information necessary to perform a first perfusion test. This is done in
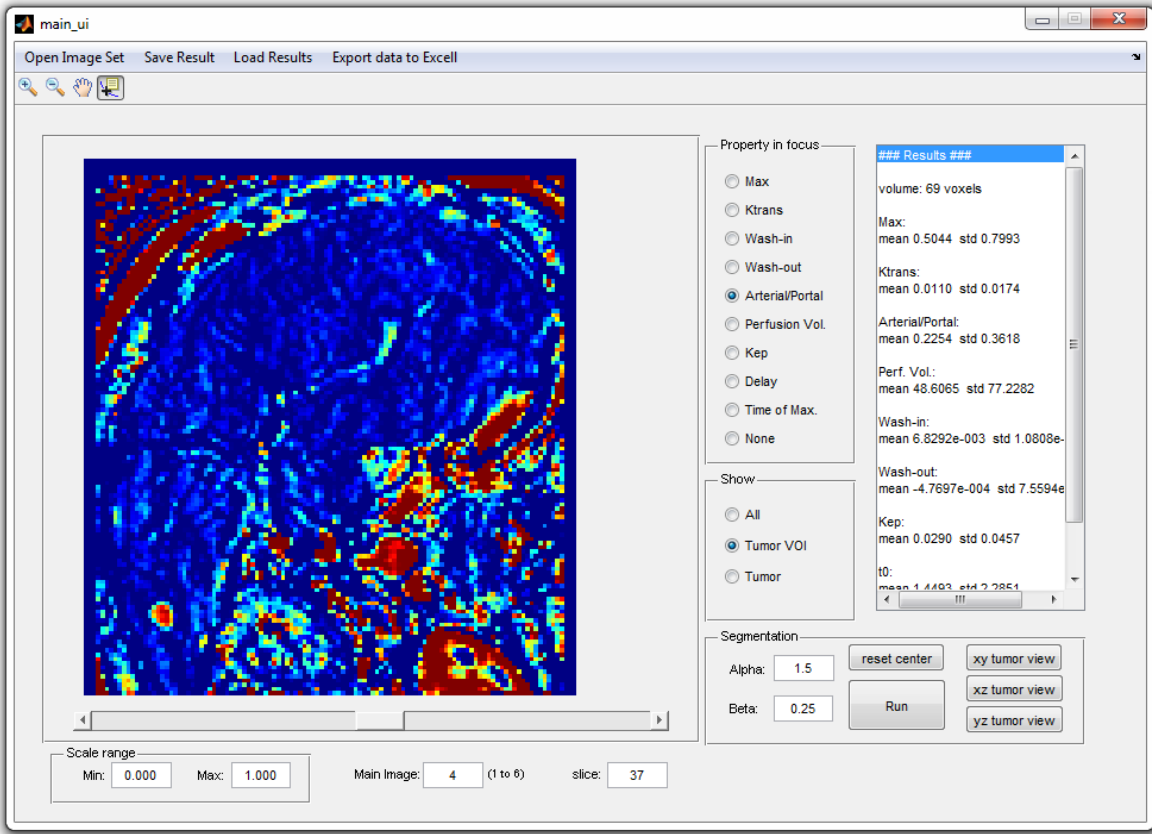
Figure 4.1: User Interface - main window

the perfusion window by means of controlling the input functions parameter limits and initial guess. The user accompanies the effects caused by the changes inferred to the model in the two axes and in the results section.

- After finishing the calibration process the 'tumor ROI' may be redefined. The volume selected should contain the tumor at its center and include a certain margin.

- The analysis starts as the user pushes the 'OK' button in the perfusion window. Since this can take from 2 minutes to several hours, depending on the number of voxels included in the tumor region, a simple bar showing the time predicted for the end of the analysis was included.

- When this task is concluded, the user may now assess the perfusion maps calculated in the main window.

- After viewing all the images, the segmentation should be performed with the image where the tumor limits are more easily identified. This can be either one of the 6 initial images or one of the parameter maps obtained.

- Then, the user defines the segmentation parameters (α, β) and accompanies the effects by comparing the region selected with the original image. The user can also view the projections of the tumor in the 3 main planes: x0y, x0z and y0z.

-Finally, the tumor mean parameters can be viewed in the results part of the main-window. The option to export the list of parameters obtained into an Excel spread sheet was also included.
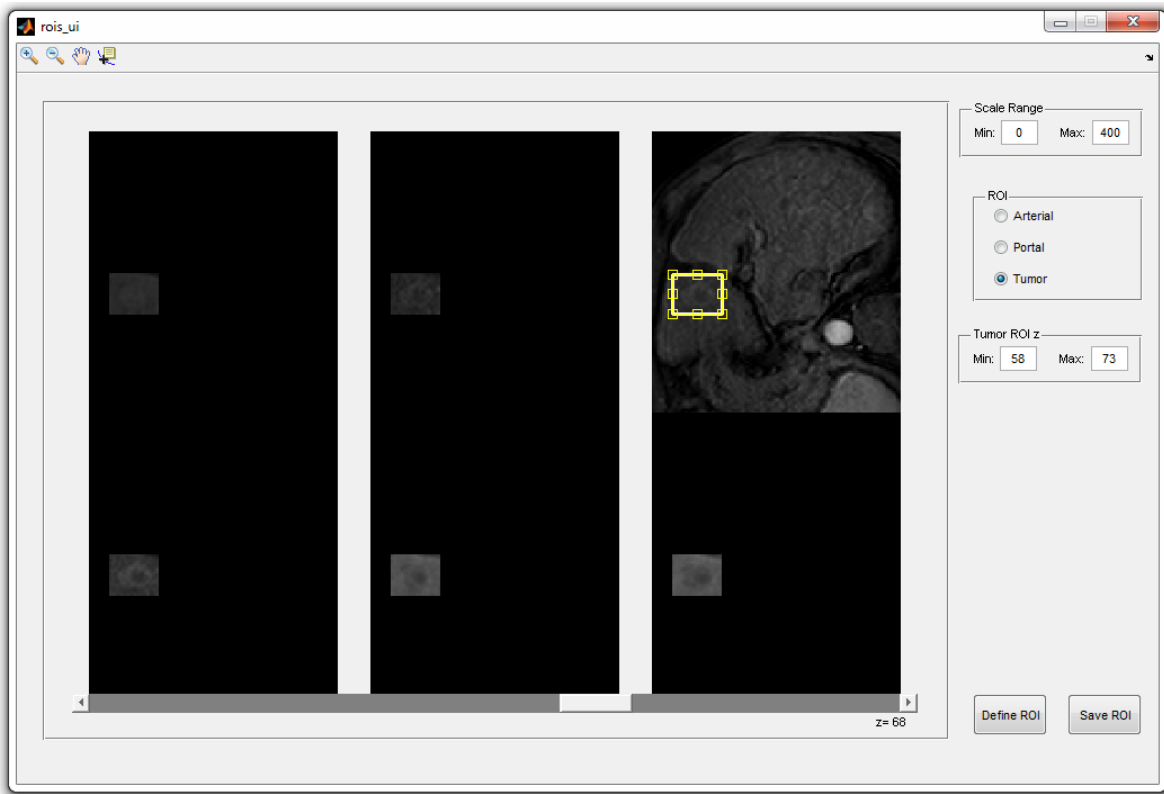
Figure 4.2: User Interface - ROIs window
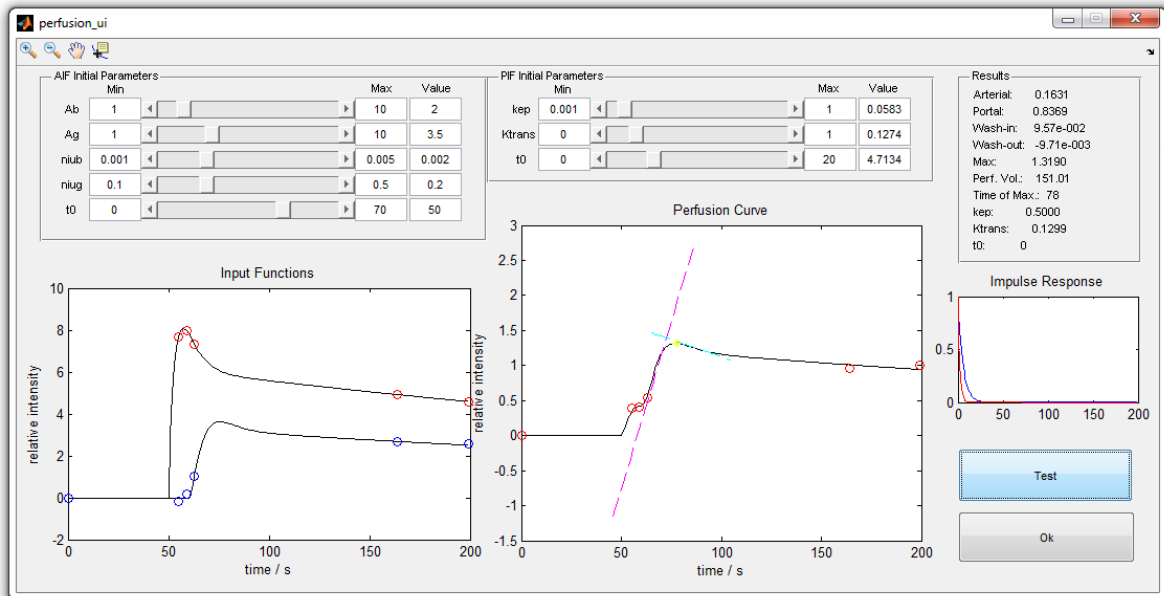
Figure 4.3: User Interface - perfusion window

33

Chapter 5

Results

The results are shown in accordance with the algorithm organization. As so, their presentation starts with the input functions obtained for each patient, followed by the parameter maps calculated for all tumor ROI analyzed. After this, the segmentation results are presented. The chapter ends with a summary table of the most relevant tumor characteristics found.

5.1 Input Functions

As already mentioned, the entire process needs a previous definition of the three ROI: aortic, hepatic portal and tumoral. This allows obtaining the points that will be used to calculate the input functions, as well as knowing the region where the perfusion analysis will be performed. The input functions obtained are presented in figure 5.1. As it can be seen, the contrast reaches previously the aorta and, only after a certain delay, the hepatic portal vein. All AIF had higher amplitude than the corresponding PIF, except for Patient 1. This disorder may be an effect of the metastatic tumor.

These input functions were previously tested by the application of the overall method in normal liver tissue. The test results are summarized in table 5.1.

Patient	Pathology	Number of voxels analyzed	Arterial ratio in liver tissue
1	Neuro-endocrine metastase	96	0.035 ± 0.068
2	Nodular Regenerative Hyperplasia	87	0.002 ± 0.011
3	Focal Nodular Hyperplasia	88	0.014 ± 0.022
4	Hemangioma	95	0.149 ± 0.082
5	Hepatocellular Carcinoma	85	0.120 ± 0.076
6	Hepatocellular Carcinoma	92	0.001 ± 0.009

Table 5.1: Arterial ratios obtained after applying the model in regions of normal liver tissue. The regions were carefully chosen so that they did not contained visible vessels.

The results were considered satisfactory since the model was able to detect that the liver receives mainly blood from the portal vein. However, it should be noticed that the main purpose of this thesis is not the correct measurement of the arterial ratio in the liver, but the detection of differences in this parameter between normal tissue, benign tumors and malignant tumors. A careful analysis of liver perfusion would need a much higher temporal resolution. This can be easily understood by observing

the freedom that a perfusion curve has between the different imaging phases. The variability of the input functions obtained confirms this aspect.
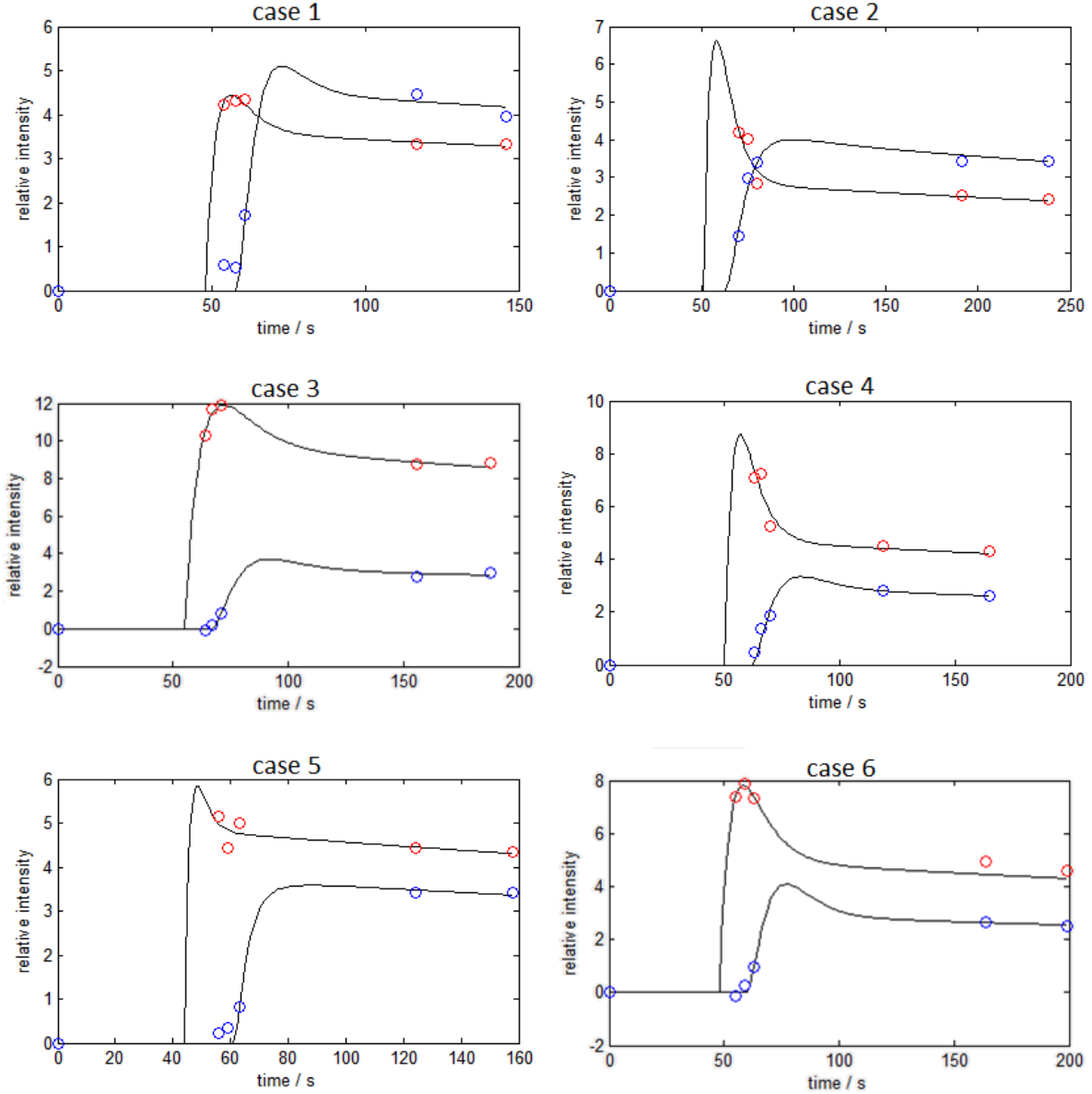
Figure 5.1: Input functions obtained for each patient. The red points correspond to the arterial signal, and the blue ones to the hepatic portal signal. The black line close to the red points corresponds to the AIF, and the other to the PIF.

5.2 Parameter Maps

The tumor regions were defined after calculating the input functions. As a result of the pharmokinetic analysis of each region, one obtains a set of 3D parameter maps. In figures 5.3 to 5.11 is shown the

main slice from the parameter maps obtained. The images are accompanied by the correspondent DCE-MRI sequence in order to allow not only a better understanding of the results, but also viewing how these perfusion images can help in the differentiation between tumors and normal tissue.

Before presenting the tumor results, there are shown two arterial ratio maps of entire slices of the liver. The examples shown contain three tumors and pretend to demonstrate the usefulness of the model in tumor detection. The arterial ratio maps were compared with the DCE-MRI image where the tumors were more easily identified.
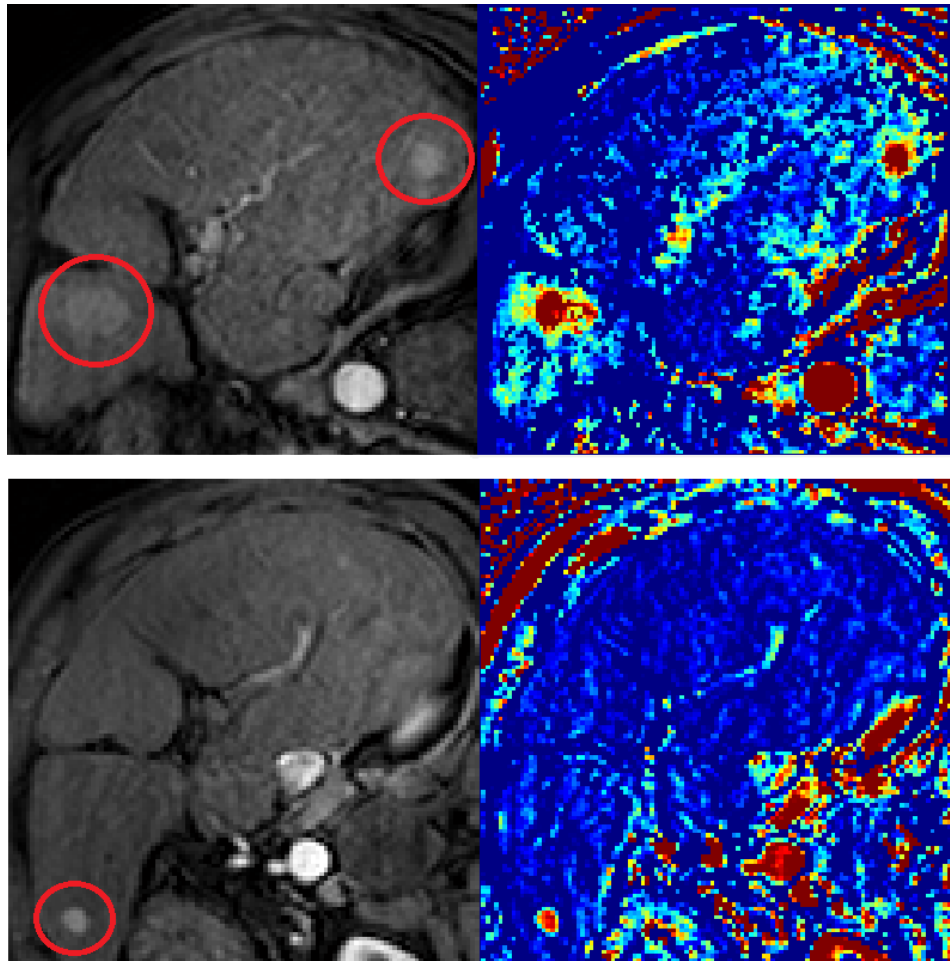

Figure 5.2: Whole liver arterial ratio analysis (right side). In the left side is presented the image where the tumor limits where more easily identified (arterial phase). The tumors (Hepatocellular Carcinoma) are signaled with a red circle.

From the parameter maps obtained several observations should be made:
- First it should be pointed out that the model used was able to identify perfusion differences between all the tumors and the surrounding liver tissue.
- Apart from the quantification of the mean arterial ratio values in each tumor, the parameter maps show clear differences between benign and malignant tissue in terms of its blood supply.
- Relatively to the other parameters, there is shown a certain relation between them and the arterial ratio. This observation may be in accordance with the physiological background in some cases, but in others it is clear that the lack of a higher temporal resolution, namely between the arterial phase

and the portal phase, allows parameters such as the wash-out rate to depend too much on the input function used.

- Relatively to the hemangioma case(figure 5.7), it remains the doubt whether the tumor is really supplied by the portal vein. It is possible that the time taken by its core to uptake contrast have erroneously caused the model to interpret this as a consequence of a low arterial ratio. Nevertheless, if we consider the tumor classification perspective, this is in accordance with the other benign tumors. On the other hand, it may actually result from an abnormal development of a hepatic portal vein branch and, in this case, it would have been interesting to analyze the model response to an liver arterial hemangioma.

- Furthermore, in terms of the perfusion volume one verifies a marked difference between big and small malignant tumors. The smaller ones are highly and homogeneously irrigated. In contrast, the accelerated growth with lack of vascular maturation causes the bigger malignant tumors to have high perfusion in their exterior and low on their core. This difficulty to perfuse the interior is reflected in almost every parameter.

- Other interesting parameter is the Time of Maximum that shows a tendency of the tumors to reach the maximum value before the rest of the liver.

- Finally, considering all the shown cases in a general way, it is noticed that malignant tumors share common features that distinguishes them from the benign ones. However, the benign lesions vary a lot depending on the underlying pathology. This may suggest that the classification should be addressed not in terms of the distinction between carcinomas and benign tumors, but directed towards the analysis of each pathology in separate. Consequently, a greater number of studies would be needed to determine the common perfusion features of each type of lesion.

More conclusions will be drawn after the identification of the tumor voxels.

5.3   Segmentation Results

After calculating the parameter maps, the tumor voxels needed to be identified. As a result, the image where the tumor had the best contrast was chosen and the segmentation performed. This process needs the parameters α and β to be consecutively tested so that a good result may be obtained.

The results obtained from the Region Growing segmentation are visible in figure 5.12. In these tumor projections is possible to detect some heterogeneity in the shape of the large malignant tumors. However the largest and more irregular shape is found in a benign 'tumor' (Patient 2 Tumor 1). In fact, this mass is a conglomerate of multiple regenerative hyperplasia nodules, what explains its appearance.

5.4   Tumor Results

The complete set of parameters obtained for each tumor is attached to this thesis. In table 5.2 were included the most relevant results in terms of the tumor classification.

Before commenting the results, it should be stated that the perfusion volumes shown represent simply the integral of the perfusion curves. Consequently they depend on the time of acquisition, as well as on the time at which the contrast was injected, what jeopardizes a inter-tumoral comparison of these values. As a result, it was introduced the liver perfusion volume in order to allow the calculation of the corresponding tumor/liver ratio. A greater ratio value should mean that, in comparison with the liver, more contrast is detected in that tissue during the same time. This is related to the contrast uptake and residence time.

Overall, the referred ratio was smaller in the malignant tumors. This may express a higher wash-out rate in malignant tumors and a perfusion decrease especially in larger ones. More tests should be performed with the purpose of determining the ability of this ratio to help in tumor characterization.

In terms of the big carcinomas found in patients 1 and 5, the small ratio values may reveal the presence of necrotic tissue.

Relatively to the arterial ratio, this revealed to be the distinguishing parameter in terms of malignancy. Benign tumors had mean arterial ratios between 16.6% and 37.5%. On the contrary malignant tumors revealed an arterial component in the range of 51.4% to 75.5%. These results are in accordance with the known information about the liver malignant tumors: these tend to develop an arterial based vasculature.

Patient	Tumor	Ben./ Malig.	Volume (cm^3)	Diam. (cm)	Arterial ratio	Tum. Mean Perf. Vol.	Liv. Mean Perf.Vol.	Perf. ratio (Tum./Liv.)
1		M	35.12	4.06	0.608 ± 0.471	7.03	15.55	0.45
2	1	B	326.33	8.54	0.202 ± 0.206	116.10	26.16	4.44
2	2	B	3.07	1.80	0.168 ± 0.166	117.76	26.16	4.50
3		B	6.26	2.29	0.375 ± 0.245	152.88	88.69	1.72
4		B	17.49	3.22	0.166 ± 0.208	263.23	85.62	3.07
5	1	M	73.28	5.19	0.660 ± 0.422	21.68	86.04	0.25
5	2	M	0.93	1.21	0.736 ± 0.175	147.35	86.05	1.71
5	3	M	2.40	1.66	0.755 ± 0.211	146.29	86.05	1.70
6		M	25.11	3.63	0.514 ± 0.362	86.18	36.32	2.37

Table 5.2: Summary table of the most relevant parameters in a tumor classification perspective. The mean tumor arterial ratios are shown together with the corresponding standard deviation (std).The tumor mean diameter was calculated considering a perfect sphere. The calculation of the tumor dimensions considered the voxel dimensions and spacing between slices. Pathology abbreviations used: *Met* - Metastase; *NRH* - Nodular Regenerative Hyperplasia; *FNH* - Focal Nodular Hyperplasia; *Hem* - Hemangioma; *HCC* - Hepatocellular Carcinoma.
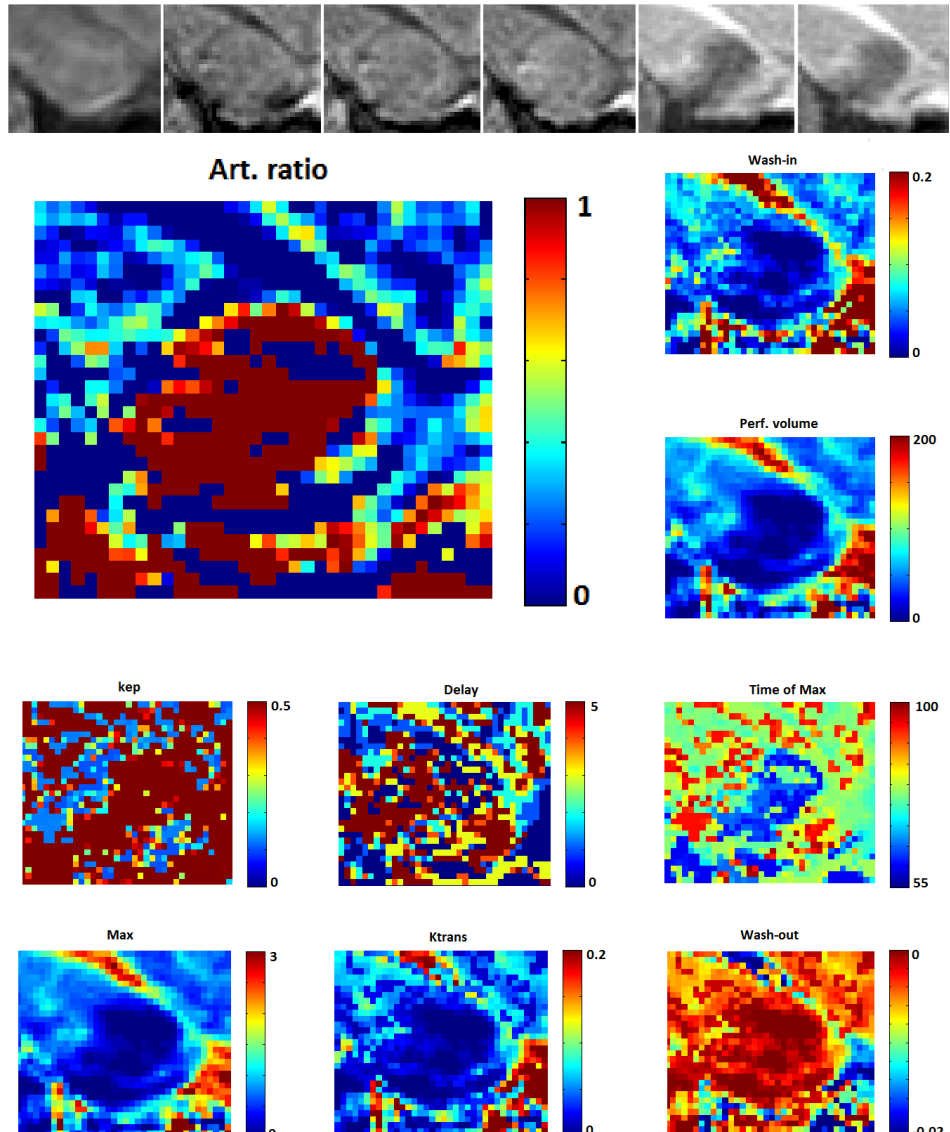
Figure 5.3: Parameter maps obtained for the neuro-endocrine metastase found in patient 1.(malignant)
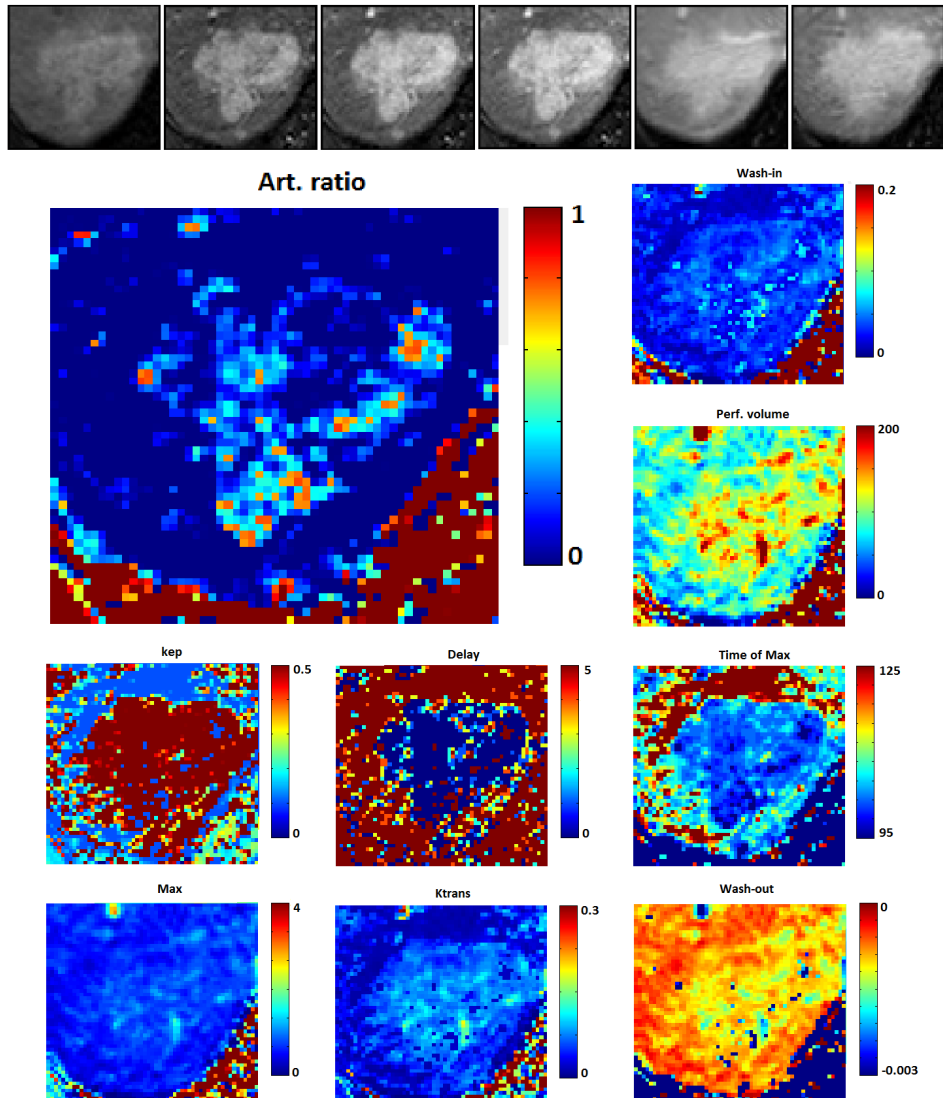
Figure 5.4: Parameter maps obtained for a regenerative hyperplasia conglomerate nodule (tumor 1) found in patient 2.(benign)
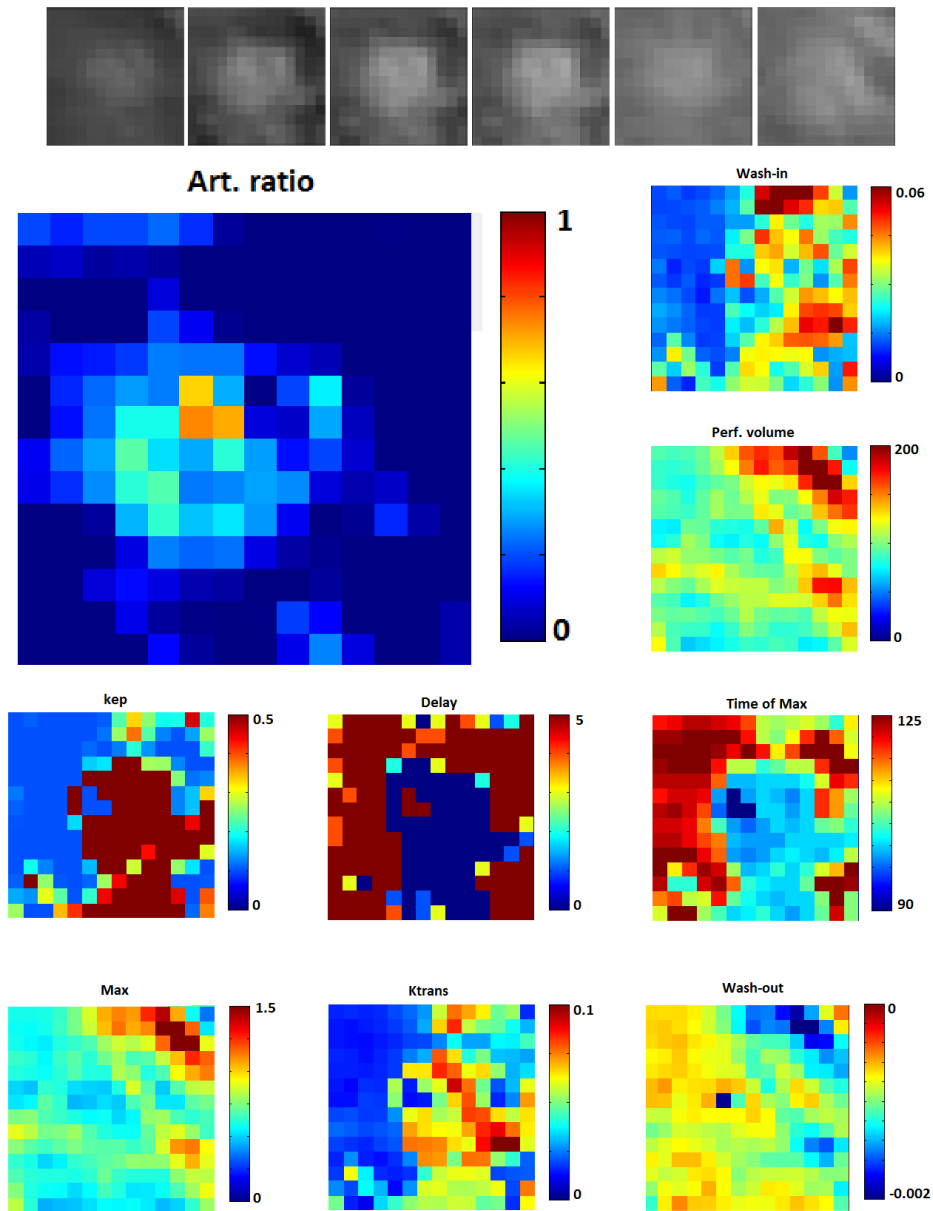
Figure 5.5: Parameter maps obtained for a regenerative hyperplasia nodule (tumor 2) found in patient 2.(benign)
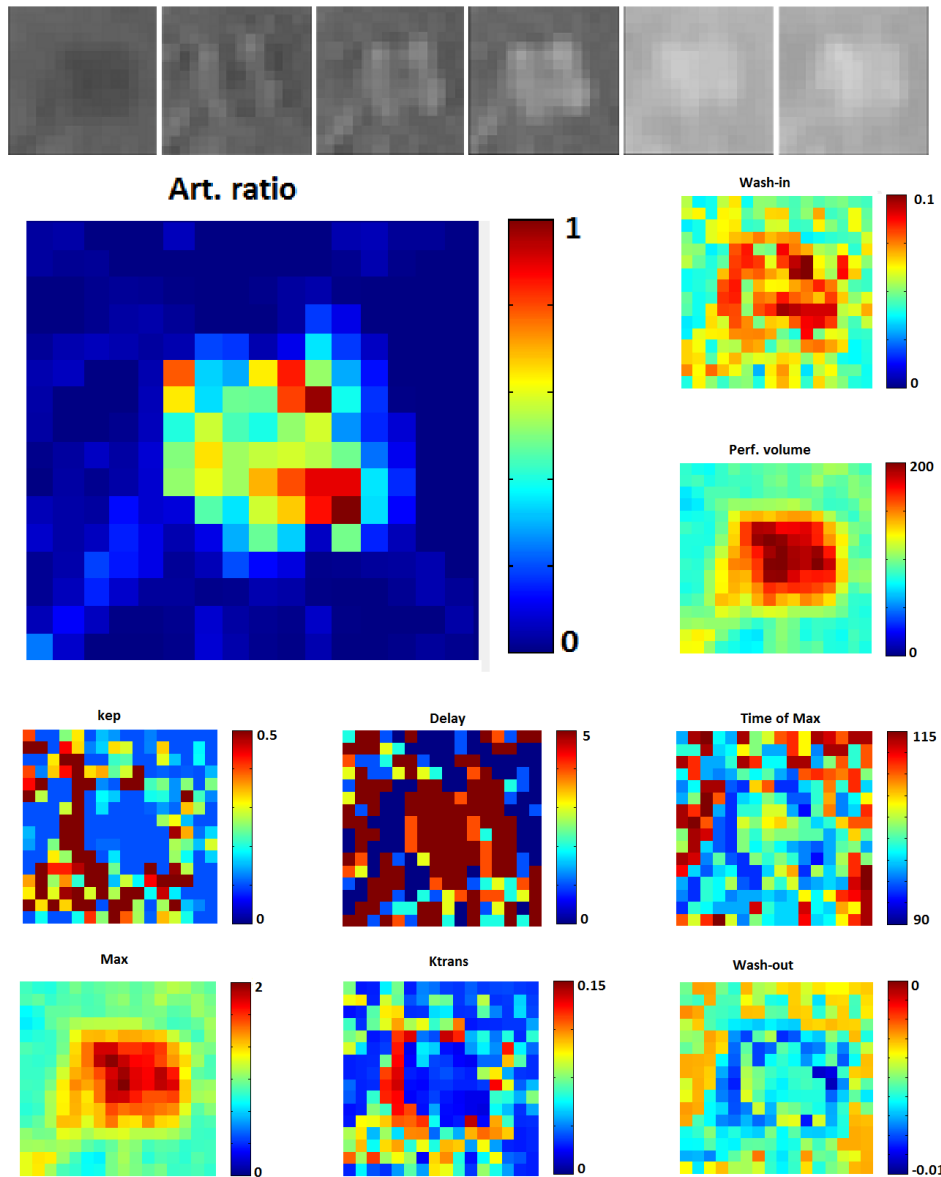
Figure 5.6: Parameter maps obtained for an exemplar of a focal nodular hyperplasia tumor found in patient 3.(benign)
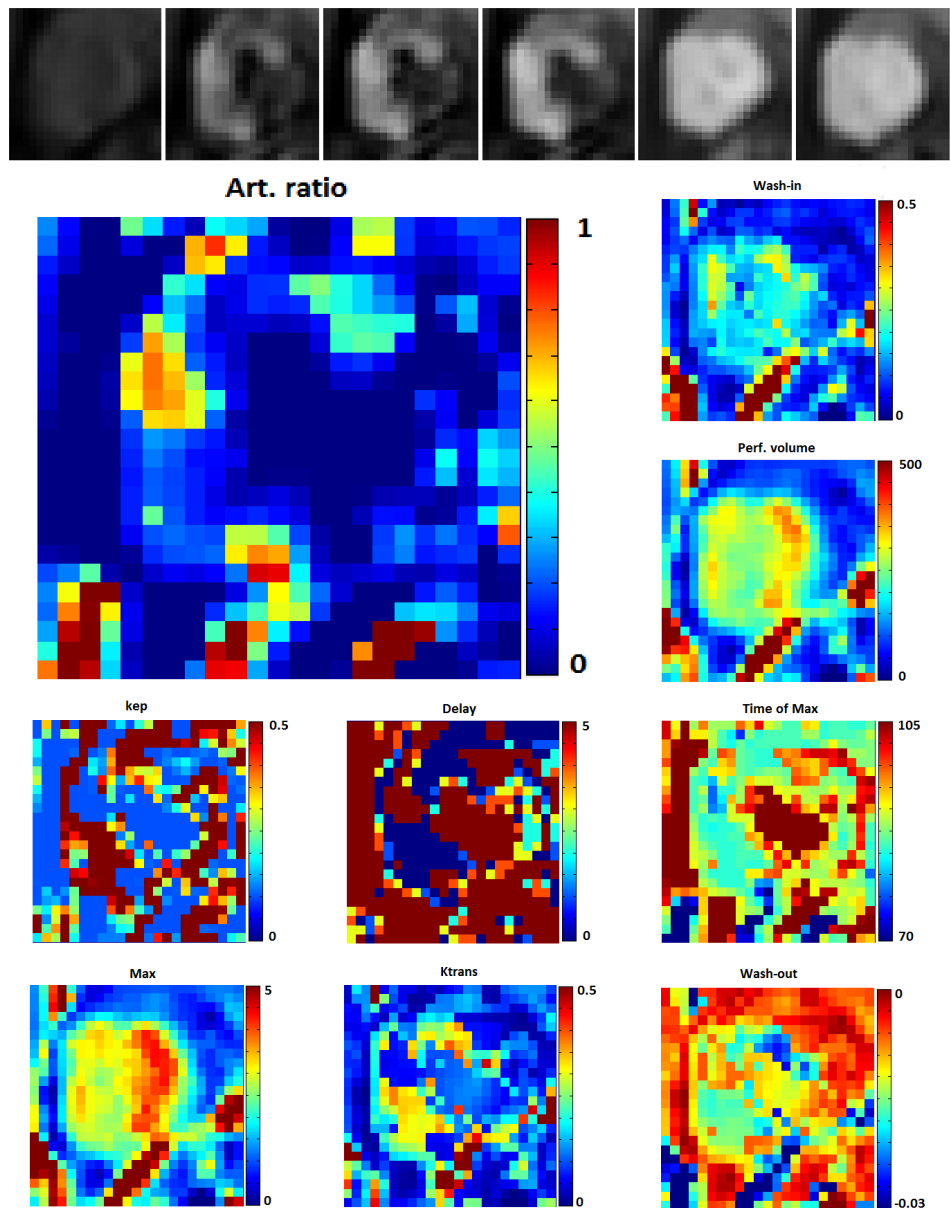
Figure 5.7: Parameter maps obtained for an hemangioma found in patient 4.(benign)
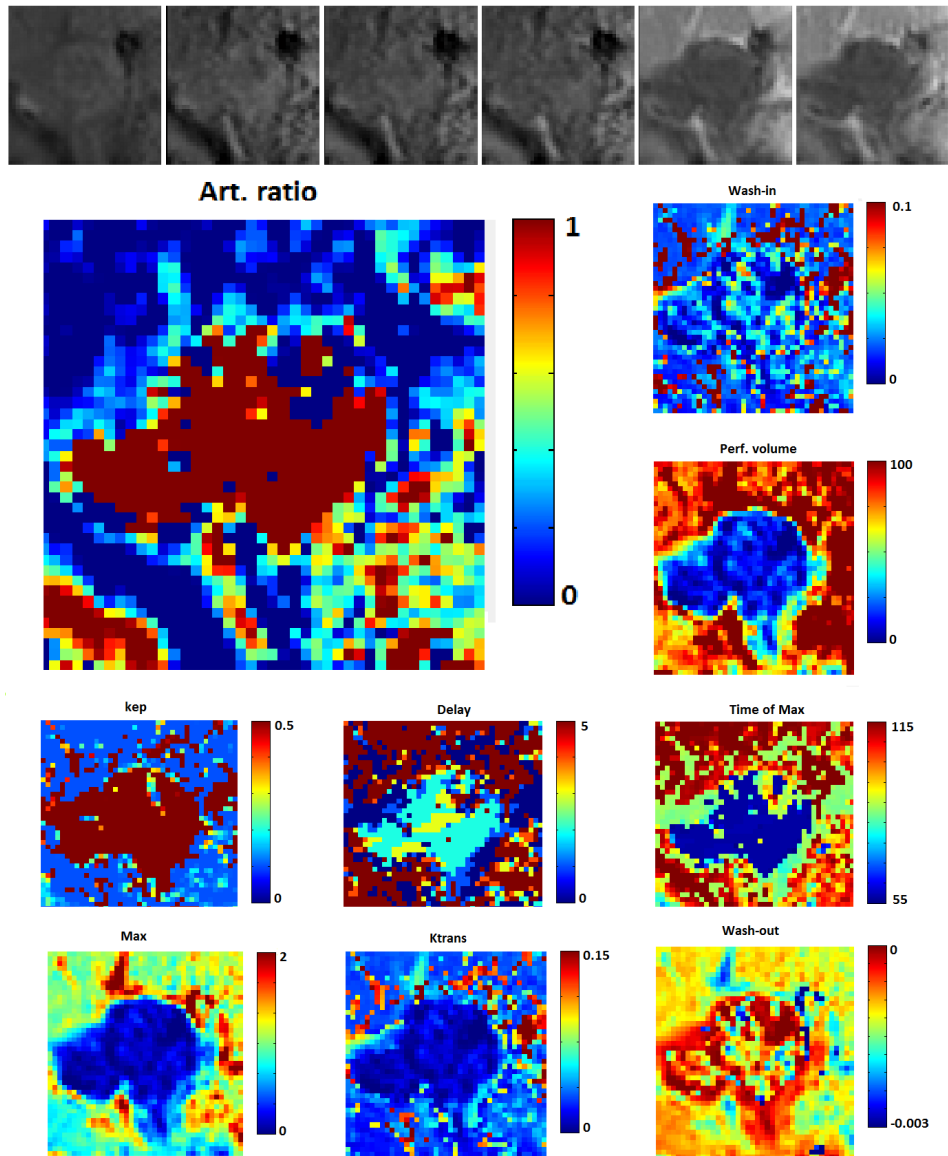
Figure 5.8: Parameter maps obtained for an exemplar of an HCC tumor (tumor 1) found in patient 5.(malignant)
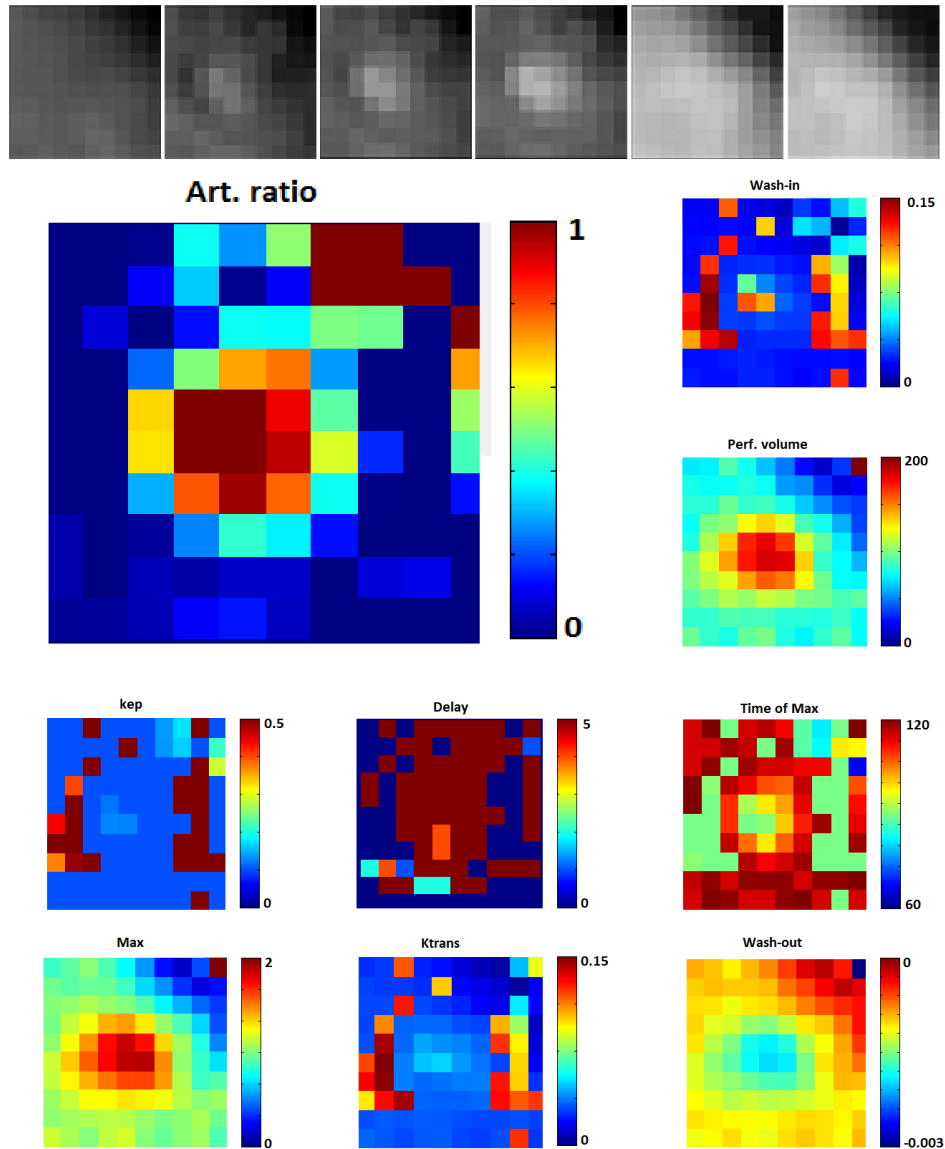
Figure 5.9: Parameter maps obtained for an exemplar of an HCC tumor (tumor 2) found in patient 5.(malignant)
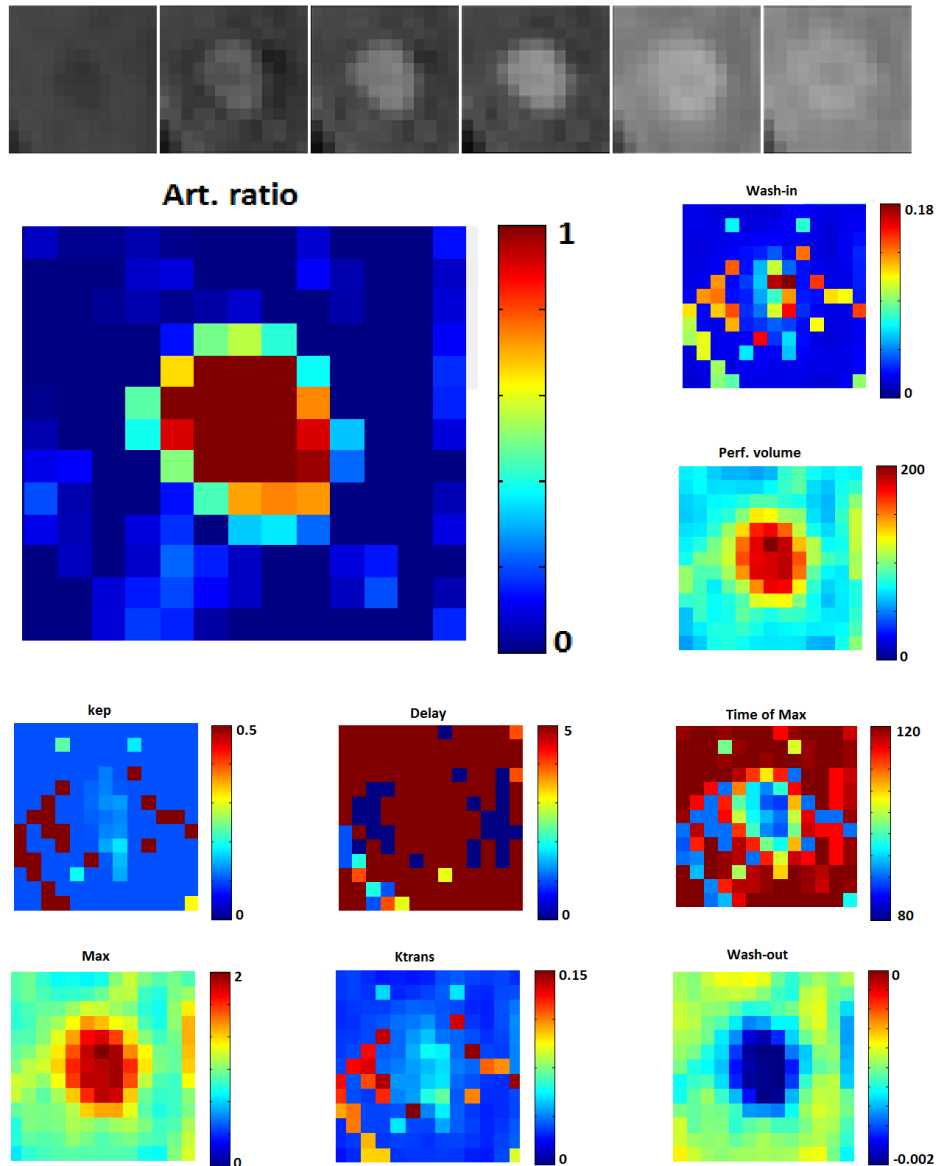
Figure 5.10: Parameter maps obtained for an exemplar of an HCC tumor (tumor 3) found in patient 5.(malignant)
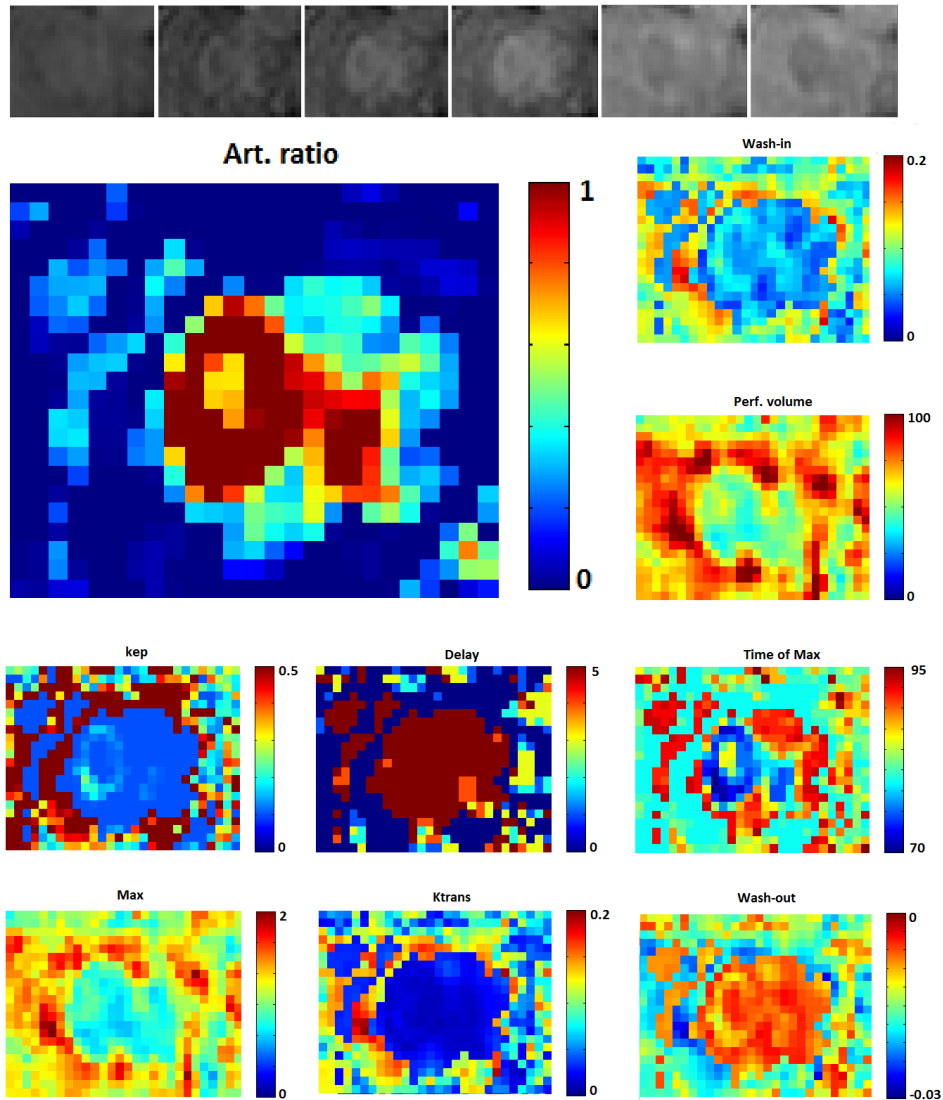
Figure 5.11: Parameter maps obtained for an exemplar of an HCC tumor found in patient 6.(malignant)
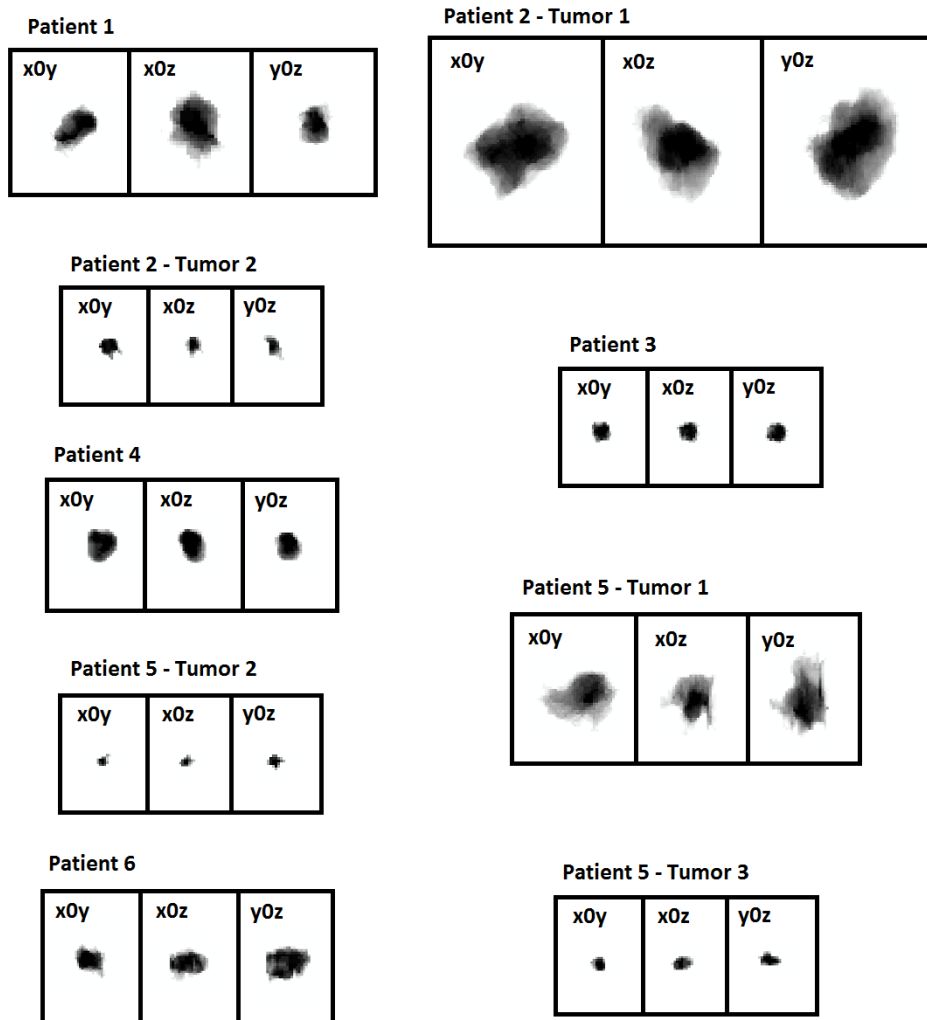
Figure 5.12: Projections of the tumor segmentated regions in the planes x0y, x0z and y0z.

Chapter 6

Conclusions and Future Work

This thesis had as initial objective the development of a method capable of classifying liver tumors in terms of its malignancy. The approach to be developed should calculate the perfusion curves of the tumors and use the information contained in them for the classification.

In order to gain insight into pharmokinetic tumor analysis, several subjects needed to be studied. These included the imaging technique (DCE-MRI), the liver morphology and vascularization, the main aspects of the tumors found in the liver and the main methods used to model tissue perfusion. Moreover, the image alignment was also approached, being this a pre-requisite for a voxel-by-voxel analysis of an image set.

Based on all the information collected, a strategy to assess liver tumor perfusion data was developed. This consisted of three main steps: Image Pre-Processing, where the images were prepared for the analysis; Retrievement of Perfusion Data, which was done by the application of the pharmokinetic model; Analysis of Results, where the information obtained from benign and malignant was compared.

Having fixed the strategy it was needed to put it into practice. Consequently, the several components of the algorithm were developed and a Graphical User Interface was created. The corresponding application emerged not only as way to implement the method but also as a tool to manage the images and perform the analysis.

Concluded the implementation, the program was tested using 6 DCE-MRI Images with confirmed diagnosis (hospital Erasme, Brussels).

The results obtained showed that the model was capable of detecting differences between normal liver tissue, benign and malignant tumors. Here the arterial ratio parameter played the main role. The strategy used was able do detected a higher contribution of the hepatic artery in the perfusion of malignant tumors. The differences between benign and malignant lesions, in terms of the blood supply, were clear. The arterial ratio obtained from these two groups gave origin to two separate intervals.

Moreover, the analysis was performed in two complete slices of the liver. In these images three tumors were evidenced, demonstrating that the ability to resolve hepatic arterial and portal components of the blood, in the liver, can be useful in tumor detection and play an important role in applications such as risk population screening.

In terms of the other parameters, these provided interesting physiological data concerning the tumor perfusion. In almost every parameter map it is possible to distinguish differences between the tumor and the surrounding tissue. Nevertheless the distinction of malignant features was not so clear as in the arterial ratio maps. This may be a consequence of the lack of a higher temporal resolution. The determination of the perfusion curves, with image sequences of only 6 acquisitions in about 3 minutes, gives the fitting process more freedom than the one desired. Consequently, parameters gain a certain variability that not only masks the distinguishing features but also jeopardize the use of the model in perfusion quantification. Besides this, the model was able to identify the arterial and portal perfusion

patterns allowing the distinction between malignant and benign tumors. This fact may indicate that very interesting results may be obtained with high temporal resolution DCE-MRI images.

In conclusion, the main strength of this thesis consists in demonstrating the importance of considering the liver dual-blood supply in liver perfusion models. This is confirmed by the successful application of such a model to low temporal resolution DCE-MRI images. Moreover, it was shown the huge amount of data that can be retrieved from dynamic contrast images.

The development of this thesis allowed a reflection concerning the directions that pharmacokinetic analysis shall follow in a near future. The evolution of rapid volume acquisitions that will allow precise perfusion measurements, together with the standardization of perfusion models used, should lead different research centers to create perfusion parameters databases. Moreover, the collection and sharing of this perfusion information in a global basis shall provide the means to an early, reliable and non-invasive tumor detection.

In cancer, the time of detection has a major influence in the chances of survival. As so, the use of such strategies in screening applications has the potential to save a considerable number of lives worldwide.

Bibliography

[1] S. Aime and P. Caravan. Biodistribution of gadolinium-based contrast agents, including gadolinium deposition. *Journal of Magnetic Resonance Imaging*, 30(6):1259–1267, 2009.

[2] A. Baert. *Encyclopedia of diagnostic imaging*. Springer Verlag, 2008.

[3] F. Bosch and J. Ribes. The epidemiology of primary liver cancer: global epidemiology. *Perspectives in Medical Virology*, 6:1–16, 2002.

[4] F. Bosch, J. Ribes, M. Díaz, and R. Cléries. Primary liver cancer: worldwide incidence and trends. *Gastroenterology*, 127(5):S5–S16, 2004.

[5] G. Brix, W. Semmler, R. Port, L. Schad, G. Layer, and W. Lorenz. Pharmacokinetic parameters in CNS Gd-DTPA enhanced MR imaging. *Journal of computer assisted tomography*, 15(4):621, 1991.

[6] G. Brix, W. Semmmler, R. Port, G. Layer, L. Schad, and W. Lorenz. Parametrization of the MRI signal enhancement during and after iv infusion of Gd-DTPA: a pharmacokinetic model. In *Society of Magnetic Resonance in Medicine*, 1990.

[7] L. Caldeira and J. Sanches. Liver tumor assessment with DCE-MRI. In *Proc. 5th IEEE International Symposium on Biomedical Imaging: From Nano to Macro*, pages 804–807, 2008.

[8] L. Caldeira and J. Sanches. Pharmacokinetic Perfusion Curves Estimation for Liver Tumor Diagnosis from DCE-MRI. *Image Analysis and Recognition*, pages 789–797, 2008.

[9] L. Caldeira, I. Silva, and J. Sanches. Automatic liver tumor diagnosis with Dynamic-Contrast Enhanced MRI. In *Image Processing, 2008. ICIP 2008. 15th IEEE International Conference on*, pages 2256–2259. IEEE, 2008.

[10] R. Cervera. Nodular regenerative hyperplasia. *Nodular Regenerative Hyperplasia*, 2005.

[11] L. Chiandussi, F. Greco, G. Sardi, A. Vaccarino, C. Ferraris, and B. Curti. Estimation of hepatic arterial and portal venous blood flow by direct catheterization of the vena porta through the umbilical cord in man. Preliminary results. *Acta hepato-splenologica*, 15(3):166, 1968.

[12] B. Choi. Vascular invasion by hepatocellular carcinoma. *Abdominal imaging*, 20(3):277–278, 1995.

[13] D. Collins and A. Padhani. Dynamic magnetic resonance imaging of tumor perfusion. *Engineering in Medicine and Biology Magazine, IEEE*, 23(5):65–83, 2004.

[14] S. Digumarthy, D. Sahani, and S. Saini. MRI in detection of hepatocellular carcinoma (HCC). *Cancer Imaging*, 5(1):20, 2005.

[15] J. Ferlay, D. Parkin, and E. Steliarova-Foucher. Estimates of cancer incidence and mortality in Europe in 2008. *European Journal of Cancer*, 46(4):765–781, 2010.

[16] B. Glocker, N. Komodakis, G. Tziritas, N. Navab, and N. Paragios. Dense image registration through MRFs and efficient linear programming. *Medical Image Analysis*, 12(6):731–741, 2008.

[17] R. C. Gonzalez and R. Woods. *Digital Image Processing 2nd Edition.* Prentice Hall, New Jersey, 2002.

[18] A. Jackson, D. Buckley, and G. Parker. *Dynamic contrast-enhanced magnetic resonance imaging in oncology.* Springer-Verlag Berlin Heidelberg, 2005.

[19] M. Jeong, J. Yu, and B. Jo. Early homogeneously enhancing hemangioma versus hepatocellular carcinoma: differentiation using quantitative analysis of multiphasic dynamic magnetic resonance imaging. *Yonsei Medical Journal*, 40:248–255, 1999.

[20] M. Knopp, F. Giesel, H. Marcos, H. von Tengg-Kobligk, and P. Choyke. Dynamic contrast-enhanced magnetic resonance imaging in oncology. *Topics in Magnetic Resonance Imaging*, 12(4):301, 2001.

[21] N. Komodakis, G. Tziritas, and N. Paragios. Fast, approximately optimal solutions for single and dynamic MRFs. In *IEEE Conference on Computer Vision and Pattern Recognition, 2007. CVPR'07*, pages 1–8, 2007.

[22] V. Kumar, A. Abbas, N. Fausto, et al. *Robbins and Cotran pathologic basis of disease.* Elsevier Saunders Philadelphia:, 2005.

[23] H. Larsson, M. Stubgaard, J. Frederiksen, M. Jensen, O. Henriksen, and O. Paulson. Quantitation of blood-brain barrier defect by magnetic resonance imaging and gadolinium-DTPA in patients with multiple sclerosis and brain tumors. *Magnetic resonance in medicine*, 16(1):117–131, 1990.

[24] I. Levy and M. Sherman. Staging of hepatocellular carcinoma: assessment of the CLIP, Okuda, and Child-Pugh staging systems in a cohort of 257 patients in Toronto. *Gut*, 50(6):881, 2002.

[25] B. Luo, Y. Wen, H. Yang, H. Zhi, B. Ou, J. Ma, J. Pan, and X. Dai. Differentiation between malignant and benign nodules in the liver: use of contrast C3-MODE technology. *World J Gastroenterol*, 11(16):2402–2407, 2005.

[26] F. Maes, A. Collignon, D. Vandermeulen, G. Marchal, and P. Suetens. Multimodality image registration by maximization of mutual information. *Medical Imaging, IEEE Transactions on*, 16(2):187–198, 2002.

[27] L. Marti-Bonmati, M. Graells, and C. Ronchera-Oms. Reduction of peristaltic artifacts on magnetic resonance imaging of the abdomen: a comparative evaluation of three drugs. *Abdominal imaging*, 21(4):309–313, 1996.

[28] R. Materne, A. Smith, F. Peeters, J. Dehoux, A. Keyeux, Y. Horsmans, and B. Van Beers. Assessment of hepatic perfusion parameters with dynamic MRI. *Magnetic Resonance in Medicine*, 47(1):135–142, 2002.

[29] M. Mescam, P. Eliat, C. Fauvel, J. Certaines, and J. Bézy-Wendling. A physiologically based pharmacokinetic model of vascular–extravascular exchanges during liver carcinogenesis: application to MRI contrast agents. *Contrast media & molecular imaging*, 2(5):215–228, 2007.

[30] G. Morana, L. Grazioli, G. Schneider, M. Testoni, K. Menni, A. Chiesa, and C. Procacci. Hypervascular hepatic lesions: dynamic and late enhancement patterns with gadobenate dimeglumine. *Acad Radiol 9 Suppl*, 2, 2002.

[31] T. Nakashima and M. Kojiro. *Hepatocellular carcinoma. An atlas of its pathology.* Springer-Verlag, Tokyo, 1987.

[32] T. Nakashima, K. Okuda, M. Kojiro, A. Jimi, R. Yamaguchi, K. Sakamoto, and T. Ikari. Pathology of hepatocellular carcinoma in Japan: 232 consecutive cases autopsied in ten years. *Cancer*, 51(5):863–877, 1983.

[33] L. Nyúl and J. Udupa. On standardizing the MR image intensity scale. *Magnetic Resonance in Medicine*, 42(6):1072–1081, 1999.

[34] T. C. of the Liver Italian Program (CLIP) Investigators. A new prognostic system for hepatocellular carcinoma: a retrospective study of 435 patients. *Hepatology*, 28:751–755, 1998.

[35] M. Orton, J. d'Arcy, S. Walker-Samuel, D. Hawkes, D. Atkinson, D. Collins, and M. Leach. Computationally efficient vascular input function models for quantitative kinetic modelling using DCE-MRI. *Physics in medicine and biology*, 53:1225, 2008.

[36] M. Orton, K. Miyazaki, D. Koh, D. Collins, D. Hawkes, D. Atkinson, and M. Leach. Optimizing functional parameter accuracy for breath-hold DCE-MRI of liver tumours. *Physics in medicine and biology*, 54:2197, 2009.

[37] A. Padhani and J. Husband. Dynamic contrast-enhanced MRI studies in oncology with an emphasis on quantification, validation and human studies. *Clinical radiology*, 56(8):607–620, 2001.

[38] P. Pandharipande, G. Krinsky, H. Rusinek, and V. Lee. Perfusion imaging of the liver: current challenges and future goals. *Radiology*, 234(3):661, 2005.

[39] F. Perez-Ruiz, F. Orte Martinez, A. Zea Mendoza, L. del Arbol, and A. Caparros. Nodular regenerative hyperplasia of the liver in rheumatic diseases: report of seven cases and review of the literature. In *Seminars in arthritis and rheumatism*, pages 47–54. Elsevier, 1991.

[40] F. Perez-Ruiz, A. Zea Mendoza, and F. Orte Martinez. Antiphospholipid antibodies may play a role in pathogenesis of nodular regenerative hyperplasia of the liver. *Br J Rheumatol*, 29(suppl 2):107, 1990.

[41] J. Pintaske, P. Martirosian, H. Graf, G. Erb, K. Lodemann, C. Claussen, and F. Schick. Relaxivity of gadopentetate dimeglumine (Magnevist), gadobutrol (Gadovist), and gadobenate dimeglumine (Multi-Hance) in human blood plasma at 0.2, 1.5, and 3 Tesla. *Investigative radiology*, 41(3):213, 2006.

[42] R. N. H. Pugh, I. M. Murray-Lyon, J. L. Dawson, M. C. Pietroni, and R. Williams. Transection of the oesophagus for bleeding oesophageal varices. *British Journal of Surgery*, 60:646649, 1973.

[43] M. Rijpkema, J. Kaanders, F. Joosten, A. van der Kogel, and A. Heerschap. Method for quantitative mapping of dynamic MRI contrast agent uptake in human tumors. *Journal of Magnetic Resonance Imaging*, 14(4):457–463, 2001.

[44] D. Rueckert, L. Sonoda, C. Hayes, D. Hill, M. Leach, and D. Hawkes. Non- rigid registration using free-form deformations: Application to breast mr images. *IEEE Transactions on Medical Imaging*, 18(8):712–721, 1999.

[45] J. Scharf, C. Zapletal, T. Hess, U. Hoffmann, A. Mehrabi, D. Mihm, V. Hoffmann, G. Brix, T. Kraus, G. Richter, et al. Assessment of hepatic perfusion in pigs by pharmacokinetic analysis of dynamic MR images. *Journal of Magnetic Resonance Imaging*, 9(4):568–572, 1999.

[46] W. Schenk Jr, J. McDonald, K. McDonald, and T. Drapanas. Direct measurement of hepatic blood flow in surgical patients: with related observations on hepatic flow dynamics in experimental animals. *Annals of surgery*, 156(3):463, 1962.

[47] A. Selwyn, E. Braunwald, D. Kasper, E. Braunwald, A. Fauci, S. Hauser, D. Longo, J. Jameson, and K. Isselbacher. *Harrison's principles of internal medicine*. McGraw-Hill Europe, 2004.

[48] R. Semelka, D. Martin, C. Balci, and T. Lance. Focal liver lesions: Comparison of dual-phase CT and multisequence multiplanar MR imaging including dynamic gadolinium enhancement. *Journal of Magnetic Resonance Imaging*, 13(3):397–401, 2001.

[49] H. Taniguchi, T. Daidoh, Y. Shioaki, and T. Takahashi. Blood supply and drug delivery to primary and secondary human liver cancers studied with in vivo bromodeoxyuridine labeling. *Cancer*, 71(1):50–55, 1993.

[50] P. Tofts. Modeling tracer kinetics in dynamic Gd-DTPA MR imaging. *Journal of Magnetic Resonance Imaging*, 7(1):91–101, 1997.

[51] P. Tofts, G. Brix, D. Buckley, J. Evelhoch, E. Henderson, M. Knopp, H. Larsson, T. Lee, N. Mayr, G. Parker, et al. Estimating kinetic parameters from dynamic contrast-enhanced T1-weighted MRI of a diffusable tracer: standardized quantities and symbols. *Journal of Magnetic Resonance Imaging*, 10(3):223–232, 1999.

[52] P. Tofts and A. Kermode. Measurement of the blood-brain barrier permeability and leakage space using dynamic MR imaging. 1. Fundamental concepts. *Magnetic Resonance in Medicine*, 17(2):357–367, 1991.

[53] G. Tortora and S. Grabowski. *Introduction to the human body: the essentials of anatomy and physiology*. John Wiley & Sons, 2004.

[54] H. Weinmann, M. Laniado, and W. Mutzel. Pharmacokinetics of GdDTPA/dimeglumine after intravenous injection into healthy volunteers. *Physiol Chem Phys Med NMR*, 16(2):167–172, 1984.

[55] Y. Yamashita, K. Mitsuzaki, T. Yi, I. Ogata, T. Nishiharu, J. Urata, and M. Takahashi. Small hepatocellular carcinoma in patients with chronic liver damage: prospective comparison of detection with dynamic MR imaging and helical CT of the whole liver. *Radiology*, 200(1):79, 1996.

[56] S. Zachow. http://public.beuth-hochschule.de/ stevie/mod+sim/node32.html, July 1997.

[57] B. Zhang, B. Yang, and Z. Tang. Randomized controlled trial of screening for hepatocellular carcinoma. *Journal of cancer research and clinical oncology*, 130(7):417–422, 2004.

Patient	Tumor	Path.	Ben./Malig.	Volume (cm^3)	Diam. (cm)	Arterial ratio	std	Tum. Perf. Vol.	std	Max	std	K_L^{trans}	std	Wash-in	std
1		Met	M	35.12	4.06	0.608	0.471	7.029	12.434	0.091	0.161	0.007	0.013	0.012	0.021
2	1	NRH	B	326.33	8.54	0.202	0.206	116.097	28.977	0.739	0.179	0.071	0.024	0.037	0.015
2	2	NRH	B	3.07	1.80	0.168	0.166	117.763	23.821	0.749	0.157	0.072	0.022	0.037	0.014
3		FNH	B	6.26	2.29	0.375	0.245	152.881	25.687	1.469	0.225	0.053	0.046	0.069	0.020
4		Hem	B	17.49	3.22	0.166	0.208	263.233	46.766	3.052	0.580	0.172	0.108	0.177	0.058
5	1	HCC	M	73.28	5.19	0.660	0.422	21.683	30.749	0.233	0.337	0.013	0.015	0.022	0.024
5	2	HCC	M	0.93	1.21	0.736	0.175	147.352	35.937	1.582	0.367	0.037	0.009	0.033	0.019
5	3	HCC	M	2.40	1.66	0.755	0.211	146.286	26.811	1.565	0.241	0.039	0.010	0.042	0.036
6		HCC	M	25.11	3.63	0.514	0.362	86.182	16.684	0.785	0.154	0.027	0.026	0.055	0.020

Table 6.1: *Summary table of perfusion parameters retrieve from the tumor analysis (part I). The mean tumor parameters are shown together with the corresponding standard deviation (std). The tumor mean diameter was calculated considering a perfect sphere. The calculation of the tumor dimensions considered the voxel dimensions and spacing between slices. Arterial ratio and K_L^{trans} result from fitting the equations (3.9) and (3.10) to the observed tumor voxel relative intensities. Relatively to the other parameters: Tumor Perfusion Volume is the integral of the perfusion curve; Max is the maximum of the perfusion curve; Wash-in is the maximal derivative found before the maximum. Pathology abbreviations used: Met - Metastase; NRH - Nodular Regenerative Hyperplasia; FNH - Focal Nodular Hyperplasia; Hem - Hemangioma; HCC - Hepatocellular Carcinoma.*

Patient	Tumor	Path.	Ben./ Malig.	Volume (cm^3)	Diam. (cm)	Wash-out	std	k_L	std	delay	std	Max time	std
1		Met	M	35.12	4.06	-8.51E-04	1.50E-03	0.472	0.087	2.052	2.115	69.538	8.815
2	1	NRH	B	326.33	8.54	-1.20E-03	8.45E-04	0.460	0.114	0.717	1.569	99.615	6.796
2	2	NRH	B	3.07	1.80	-1.03E-03	2.35E-04	0.461	0.111	0.342	1.100	101.370	4.157
3		FNH	B	6.26	2.29	-6.04E-03	1.64E-03	0.220	0.167	3.621	2.089	99.819	44.793
4		Hem	B	17.49	3.22	-1.30E-02	4.86E-03	0.226	0.156	3.066	2.295	94.617	8.308
5	1	HCC	M	73.28	5.19	-6.57E-04	6.79E-04	0.406	0.164	2.261	1.717	74.294	22.948
5	2	HCC	M	0.93	1.21	-1.63E-03	3.83E-04	0.103	0.008	4.804	0.483	105.036	6.176
5	3	HCC	M	2.40	1.66	-1.62E-03	2.63E-04	0.109	0.020	5.000	0.000	103.035	8.131
6		HCC	M	25.11	3.63	-6.60E-03	3.15E-03	0.172	0.138	3.954	1.916	84.067	6.478

Table 6.2: *Summary table of perfusion parameters retrieve from the tumor analysis (part II). The mean tumor parameters are shown together with the corresponding standard deviation (std).The tumor mean diameter was calculated considering a perfect sphere. The calculation of the tumor dimensions considered the voxel dimensions and spacing between slices. Delay and k_L result from fitting the equation (3.9) to the observed tumor voxel relative intensities. Relatively to the other parameters: Max time is the time at which the maximum of the perfusion curve occurs; Wash-out is the minimal derivative found after the maximum. Pathology abbreviations used: Met - Metastase; NRH - Nodular Regenerative Hyperplasia; FNH - Focal Nodular Hyperplasia; Hem - Hemangioma; HCC - Hepatocellular Carcinoma.*